

### Public Domain Mark 1.0 Universal

This work was written as part of one of the author's official duties as an Employee of the United States Government and is therefore a work of the United States Government. In accordance with 17 U.S.C. 105, no copyright protection is available for such works under U.S. Law.

Access to this work was provided by the University of Maryland, Baltimore County (UMBC) ScholarWorks@UMBC digital repository on the Maryland Shared Open Access (MD-SOAR) platform.

### **Please provide feedback**

Please support the ScholarWorks@UMBC repository by emailing [scholarworks-group@umbc.edu](mailto:scholarworks-group@umbc.edu) and telling us what having access to this work means to you and why it's important to you. Thank you.



# FRAMEx. V. Radio Spectral Shape at Central Subparsec Region of Active Galactic Nuclei

Onic I. Shuvo<sup>1,2</sup>, Megan C. Johnson<sup>2</sup>, Nathan J. Secrest<sup>2</sup>, Mario Gliozzi<sup>3</sup>, Phillip J. Cigan<sup>2</sup>, Travis C. Fischer<sup>4</sup>, and Alexander J. Van Der Horst<sup>5</sup>

<sup>1</sup> Department of Physics, University of Maryland Baltimore County, 1000 Hilltop Circle, Baltimore, MD 21250, USA; [oshuvo@gmu.edu](mailto:oshuvo@gmu.edu)

<sup>2</sup> U.S. Naval Observatory, 3450 Massachusetts Avenue NW, Washington, DC 20392-5420, USA

<sup>3</sup> Department of Physics and Astronomy, George Mason University, MS3F3, 4400 University Drive, Fairfax, VA 22030, USA

<sup>4</sup> AURA for ESA, Space Telescope Science Institute, 3700 San Martin Drive, Baltimore, MD 21218, USA

<sup>5</sup> Department of Physics, The George Washington University, 725 21st Street NW, Washington, DC 20052, USA

Received 2023 July 15; revised 2023 December 5; accepted 2023 December 6; published 2024 January 18

## Abstract

We present results from the Very Long Baseline Array multifrequency (1.6, 4.4, 8.6, and 22 GHz), high-sensitivity ( $\sim 25 \mu\text{Jy beam}^{-1}$ ), subparsec-scale ( $< 1 \text{ pc}$ ) observations and spectral energy distributions for a sample of 12 local active galactic nuclei (AGNs), a subset from our previous volume-complete sample with hard-X-ray (14–195 keV) luminosities above  $10^{42} \text{ erg s}^{-1}$ , out to a distance of 40 Mpc. All 12 of the sources presented here were detected in the *C* (4.4 GHz) and *X* (8.6 GHz) bands, 75% in the *L* band (1.6 GHz), and 50% in the *K* band (22 GHz). Most sources showed compact, resolved/slightly resolved, central subparsec-scale radio morphology, except for a few with extended outflow-like features. A couple of sources have an additional component that may indicate the presence of a dual-core, single or double-sided jet or a more intricate feature, such as radio emission resulting from interaction with the nearby interstellar medium. The spectral slopes are mostly gigahertz-peaked or curved, with a few showing steep, flat, or inverted spectra. We found that at the subparsec scale, the gigahertz-peaked spectra belong to the low-accreting, radio-loud AGNs, with a tendency to produce strong outflows, possibly small-scale jets, and/or have a coronal origin. In contrast, flat/inverted spectra suggest compact radio emission from the central regions of highly accreting AGNs, possibly associated with radio-quiet AGNs producing winds/shocks or nuclear star formation in the vicinity of black holes.

*Unified Astronomy Thesaurus concepts:* Active galaxies (17); Extragalactic radio sources (508); Radio galaxies (1343); Radio jets (1347); Active galactic nuclei (16)

## 1. Introduction

An active galactic nucleus (AGN) generates enormous power. It radiates throughout the electromagnetic spectrum from radio to gamma rays due to the accretion of matter onto the supermassive black hole (SMBH) residing at its center. To monitor and observe such powerful and luminous hearts of active galaxies, the U.S. Naval Observatory (USNO), in collaboration with a few other institutions, is conducting the Fundamental Reference AGN Monitoring Experiment, or FRAMEx (Dorland et al. 2020). Using ground- and space-based telescopes, FRAMEx is observing a sample of nearby AGNs in the X-ray and radio wavelengths at multiple epochs to understand and characterize their physical properties.

In the first paper on FRAMEx, Fischer et al. (2021, hereafter Paper I) tested the “fundamental plane of black hole activity” (FP; e.g., Merloni et al. 2003; Gültekin et al. 2009), the apparent correlation between radio emission (6 GHz), X-ray emission (2–10 keV), and black hole mass ( $M_{\text{BH}}$ ), using simultaneous Swift X-ray Telescope and Very Long Baseline Array (VLBA) radio observations of 25 local AGNs. If it held, it would support the unification of AGN accretion physics in conflict with the purported radio-loud (RL)/radio-quiet (RQ) dichotomy (Hutchings et al. 1989; Miller et al. 1990; Antonucci 1993). But it was found that the FP breaks down

when probing the innermost regions of AGNs in milliarcsecond (subparsec) scales. In contrast, the extended extranuclear radio emission (tens to hundreds of parsecs) measured from archival Jansky Very Large Array (VLA) observations is responsible for the apparent FP correlation. A few other FRAMEx results provided intriguing motivation for a natural extension of our earlier observations. For example, only three of nine sources were detected in a follow-up campaign (Shuvo et al. 2022, hereafter Paper III) with higher observing sensitivity ( $\sim 10 \mu\text{Jy}$ ) of initially undetected sources (from Paper I) at 6 GHz, despite reaching noise levels  $\sim$ two times below the predicted rms from the VLA detections ( $\sim 50 \mu\text{Jy}$ ), thus calling into question whether RQ AGNs may, in fact, be radio-silent at VLBA spatial scales. In addition, a drop in apparent radio luminosity was observed for NGC 2992 in our first simultaneous X-ray and radio variability campaign (Fernandez et al. 2022, hereafter Paper II). NGC 2992 was identified clearly in the initial 6 GHz radio survey, but during six epochs of monitoring this AGN every 28 days, we observed the luminosity fall below the detection limit during the fourth session by at least a factor of 3 and then reappear in the final two epochs. Also, the possibly discrepant extended structure of NGC 1068 across multiple epochs in the *C* band raises exciting questions about the variability of the source structure. All these results underscore the importance of obtaining quasi-simultaneous, multiwavelength radio observations to understand the physical processes that affect the apparent luminosity, variability, and morphologies of AGNs.



Original content from this work may be used under the terms of the [Creative Commons Attribution 4.0 licence](https://creativecommons.org/licenses/by/4.0/). Any further distribution of this work must maintain attribution to the author(s) and the title of the work, journal citation and DOI.

The limited accessible bandwidth of the VLBA  $C$ -band (6 GHz) observations alone precluded the determination of the radio spectral index  $\alpha$  (in this paper,  $\alpha$  is defined as  $S_\nu \propto \nu^{+\alpha}$ ), which can be used to distinguish between competing radio emission mechanisms, e.g., synchrotron versus thermal bremsstrahlung (free-free). Observations from the  $L$  ( $\sim 1.6$  GHz) to  $K$  ( $\sim 22$  GHz) bands at VLBA resolutions span the necessary frequency range to shed light on the physical processes at work in these AGNs. By utilizing source spectral indices and resolving the compact cores at higher radio frequencies, we can gain a deeper understanding of the physical nature of these systems.

Radio emission in an RL AGN is primarily caused by synchrotron emission. This occurs when highly collimated plasma jets are accelerated away from the nucleus at relativistic speeds. On the other hand, in an RQ AGN, the radio emission could be produced by a wide range of physical mechanisms, such as star formation, accretion disk winds, coronal disk emission, or low-power jets, without any significant contribution from the powerful relativistic luminous jets (Panessa et al. 2019). Following these different origins of radio emission, Paper III showed from a subparsec-scale set of VLBA observations of RQ AGNs that relativistic particles accelerated in shocks and winds or low-luminosity outflows may be a possible source of weak radio emission (and the consequent low detection rate). We demonstrated that the nondetections might result from synchrotron self-absorption at 6 cm in the radio core, similar to what has been observed in stellar-mass black holes in X-ray binaries (XRBs) while transitioning from the radiatively inefficient state to a radiatively efficient state (Coriat et al. 2011 and references therein). A well-sampled radio spectral energy distribution (SED) can help us determine the true origin of radio emission and disentangle contributions from multiple potential components.

To achieve this goal, we present results from a high-resolution, multiwavelength radio continuum emission study of 12 detected AGNs from our previous  $C$ -band campaigns (Papers I, II, and III). We obtained VLBA observations in the  $L$  ( $\sim 1.6$  GHz),  $C$  ( $\sim 4.4$  GHz),  $X$  ( $\sim 8.6$  GHz), and  $K$  ( $\sim 22$  GHz) radio bands with homogeneous observing setups (details are discussed in Section 2.2), instrument systematics, and integration to a similar sensitivity level, providing a consistent baseline from which meaningful comparisons can be made. The sample selection, multiwavelength VLBA radio observations, and data calibration details are discussed in Section 2. We present our results and discussion about the origin of the radio emission for these nearest hard-X-ray-selected AGNs in Sections 3 and 4, respectively.

## 2. Methodology

### 2.1. Sample Selection

In Paper I, we had the opportunity to observe 25 AGNs with the VLBA at milliarcsecond (subparsec) scales in  $C$  band/6 cm and detected only nine sources. Later, a follow-up observing program recovered five more sources (as described in Paper III). Three of these were detected in a deeper 4 hr on-source integration time survey, which followed up on previous nondetections. The remaining two sources were detected during observations that completed the volume-limited sample of 34 AGNs. Here, we selected 12 sources that were detected in our previous analyses, which correspond to all detected

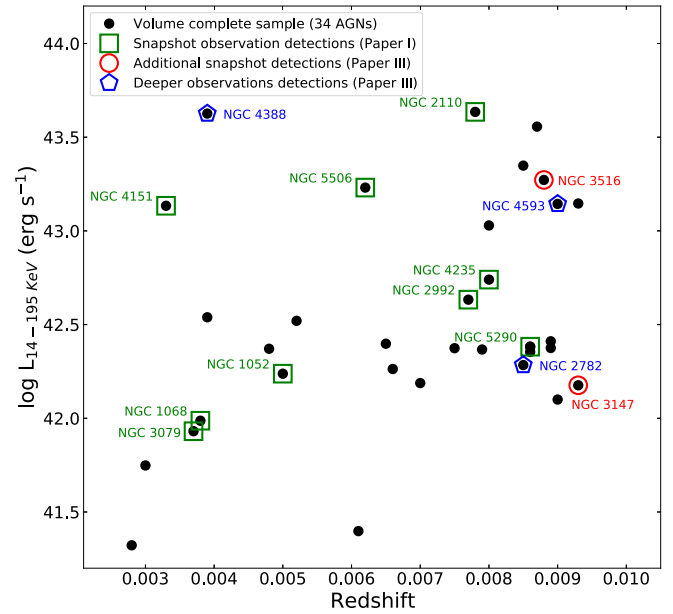


**Figure 1.** Hard-X-ray (14–195 keV) luminosity vs. redshift for our volume-complete sample of 34 nearby AGNs from the 105 month Swift Burst Alert Telescope (BAT) catalog. The green squares are the sources detected in our initial snapshot campaign (Paper I), whereas the red circles are the detected sources from our additional snapshot observation (Paper III). The blue pentagons are a subset of the Paper I sample detected in our follow-up deep-integration observations, discussed in Paper III. However, NGC 2782 and NGC 3147 were dropped from our final list of sample sources (see Section 2.2.1).

sources, except for NGC 2782 and NGC 3147, as detailed in Section 2.2, for a multiwavelength study at the  $L$ ,  $C$ ,  $X$ , and  $K$  bands with the VLBA. We illustrate our selection method in Figure 1, and sample sources, along with their global properties, are listed in Table 1.

### 2.2. VLBA Data

#### 2.2.1. Observations

Using the radio interferometry sensitivity equation and verifying with the European Very Long Baseline Interferometry (VLBI) Networks<sup>6</sup> online calculator, the on-source integration times necessary to produce images with thermal noise levels of  $\sim 25 \mu\text{Jy beam}^{-1}$  with dual polarization are estimated as 53 minutes at  $L$  band, 26 minutes at  $C$  band, 63 minutes at  $X$  band, and 4 hr at  $K$  band. We employed phase referencing for all targets except for NGC 1052, which showed a signal-to-noise ratio (S/N) of  $\sim 200$  at 6 GHz in Paper I. We adopt the nominal absolute flux density calibration error of 10% and do not require separate flux density calibration scans. We designed an efficient observing program optimized for the science goals, while allowing flexibility for easy incorporation into the dynamic scheduling process. We split the  $K$ -band observations for each target into two 4 hr segments, which can be scheduled dynamically as needed, due to the requirement for good weather. For all remaining  $L$ -band to  $X$ -band observations, we combined them into a third key file, switching between short sets of each receiver setting the spread evenly throughout a single track to maximize UV coverage. We set up the dynamic scheduling constraints such that all three schedule files per source were completed within  $\sim 24$ –48 hr to

<sup>6</sup> <http://old.evlbi.org/cgi-bin/EVNcalc.pl>

**Table 1**  
FRAMEx Multifrequency Sample

Target	R.A. (ICRS) (deg)	Decl. (ICRS) (deg)	Type	Redshift	Distance (Mpc)	$\log(M_{\text{BH}})$ ( $M_{\odot}$ )
NGC 1052	40.2699938	−8.25576443	Sy2	0.0050	21.5	8.67
NGC 1068	40.6696215	−0.01329436	Sy2	0.0038	16.3	6.93
NGC 2110	88.0474036	−7.45625207	Sy2	0.0078	33.6	9.38
NGC 2992	146.4251875	−14.32636110	Sy2	0.0077	33.2	8.33
NGC 3079	150.4911624	+55.67984716	Sy2	0.0037	15.9	6.38
NGC 3516	166.6977634	+72.56869399	Sy1.2	0.0088	37.9	7.39
NGC 4151	182.6357333	+39.40585098	Sy1	0.0033	14.2	7.55
NGC 4235	184.2911746	+7.19157594	Sy1	0.0080	34.5	7.55
NGC 4388	186.4450833	+12.66206940	Sy2	0.0039	16.8	6.94
NGC 4593	189.9143480	−5.34417639	Sy1	0.0090	38.8	6.88
NGC 5290	206.3298250	+41.71235376	Sy2	0.0086	37.1	7.78
NGC 5506	213.3119838	−3.20765470	Sy1.9	0.0062	26.7	6.96

**Note.** ICRS (a catalog of extragalactic radio sources) coordinates were retrieved from the astropy.coordinates package ([https://docs.astropy.org/en/stable/api/astropy.coordinates.get\\_icrs\\_coordinates.html](https://docs.astropy.org/en/stable/api/astropy.coordinates.get_icrs_coordinates.html)).  $M_{\text{BH}}$  values were estimated from the  $M$ – $\sigma^*$  correlation when other more direct measurements were not available, and the distances were obtained from redshift measurements (as explained in Paper I).

ensure quasi-simultaneous coverage across all the radio bands. NGC 2782, the weakest detection from our deeper observations (Paper III), was dropped because it was five times fainter than other detections in  $C$  band and only four times our estimated theoretical best rms noise floor. In addition, NGC 2782 was dropped due to being too close to the Sun during the observation period. On the other hand, NGC 3147 was observed without any phase calibrator, similar to NGC 1052, because it showed an S/N of  $\sim 150$  at 6 GHz in Paper III and was expected to be bright enough to fringe fit on itself, but it failed the fringe fitting task and thus was dropped from our final list of sample sources. The details of the VLBA multiband observation segments, including scan time, date of observation, and list of phase calibrators, are shown in Table 2.

### 2.2.2. Calibration and Imaging

We used the National Radio Astronomy Observatory Astronomical Image Processing System (AIPS; van Moorsel et al. 1996) release 31DEC19 to calibrate our VLBA data. Each frequency data set was calibrated independently by a target-phase calibrator pair (except for NGC 1052). Bad data were flagged, and calibration was performed using the standard AIPS VLBA procedures, following the prescription outlined in Paper I. We used the AIPS task IMAGR to make images of the calibrators and sources, cleaning the images until the rms approached three times the theoretical thermal noise limit. We used successive iterations of phase-only self-calibration by using the AIPS task CALIB. The process uses models produced in a previous image applied to the next iteration to improve the source phase. Self-calibration was applied to brighter sources, including NGC 1052, NGC 3079, and NGC 5506 (see Table 3 for details). In cases where self-calibration was not feasible for some or all of the four band images, a correction factor was applied to the peak intensities to prevent coherence loss (Martí-Vidal et al. 2010). A correction factor was obtained for each band by comparing other frequency data sets of the same source with and without self-calibration. The resulting value ( $\sim 10\%$ – $30\%$  of the peak intensities, based on the frequency band) was then added to the total uncertainty calculation for observations without self-calibration. Later, we applied amplitude and phase self-calibration to improve the amplitude when

necessary. Self-calibration was iterated until the image S/N improved and the ratio between bad and good solutions in the CALIB task was  $\leq 10\%$ . We achieved an S/N of  $> 10$  for most of our detections in all bands, except for a few sources where the S/N was limited to  $\leq 5$  at higher frequencies, especially in the  $K$  band. For more information on our calibration and imaging procedures, please see Sections 2.2.1 and 2.2.2, respectively, in Paper I.

## 3. Results

Table 3 lists the multiwavelength radio observation properties for our final calibrated images displayed in Figure 2 for all sources. Along with four frequency band images, we added a plot of the SED using the peak intensities ( $\log F_{\text{Gauss}}^{\text{peak}}$ ) and observed frequencies ( $\log \nu$ ) in Figure 2. The peak intensity values for all four bands were measured from CASA's 2D Gaussian model fitting algorithm. We used simple functions to characterize the SEDs in the log–log plane of peak intensity and frequency: (1) a standard power law; and (2) a best-fitting quadratic/parabola or curved power-law model (a Gaussian in nonlogarithmic space). In addition, we applied a piecewise linear regression model for sources fitted with a curved power-law model to demonstrate the spectral shape in the lower- and higher-frequency ends separately. For a single power-law spectrum, flat- and steep-spectrum radio sources are defined as having spectral indices smaller or larger than a particular limiting value, typically  $\alpha_{\text{lim}} \sim 0.5$  (Tadhunter 2016). Following the spectral index sign convention used in this paper ( $S_{\nu} \propto \nu^{+\alpha}$ ), we define a steep spectrum as having  $\alpha \leq -0.5$ , a flat one as having  $-0.5 < \alpha \leq 0$ , and an inverted spectrum as having  $\alpha > 0$ . To determine whether the radio-emitting region is an extended or a point-like source, we have added two additional SED plots for each source using peak and integrated flux density measurements only from the  $C$  and  $X$  bands. The difference between the integrated flux value and the peak intensity can provide information about the extension of the radio-emitting region. However, before making such comparisons, we applied UVTAPER in the AIPS task IMAGR to specify the widths ( $\sim 50,000$  k $\lambda$ ) in the  $U$  and  $V$  directions of the Gaussian function, which made their beam sizes comparable; thus, their integrated flux

**Table 2**  
Details of VLBA Multiband Observation Segments

Segment	Target	Obs. Band	Source Scan Time (min)	Phase Calibrator	Separation (deg)	Obs. Date Range (2021)
UC002A	NGC 3079	<i>L, C, X</i>	55, 27, 63	J1014+5503	1.85	May-3 23:24 – May-4 05:27
UC002C	NGC 4388	<i>L, C, X</i>	55, 27, 62	J1225+1253	0.28	Apr-14 03:27 – Apr-14 09:22
UC002D	NGC 4151	<i>K</i>	230	J1206+3941	0.81	May-20 23:47 – May-21 07:35
UC002E	NGC 4151	<i>L, C, X</i>	54, 27, 62	J1206+3941	0.81	May-21 23:43 – May-22 05:45
UC002F	NGC 5290	<i>K</i>	230	J1359+4011	3.10	Jun-18 23:07 – Jun-19 07:30
UC002G	NGC 5290	<i>L, C, X</i>	55, 27, 62	J1359+4011	3.10	Jun-18 00:11 – Jun-18 06:35
UC002I	NGC 5506	<i>L, C, X</i>	54, 27, 62	J1404–0130	2.72	Jun-20 00:33 – Jun-20 06:37
UC002L	NGC 1052	<i>K</i>	245	...	...	Jul-30 11:09 – Jul-30 11:09
UC002M	NGC 1052	<i>L, C, X</i>	56, 28, 64	...	...	Jul-29 11:13 – Jul-29 14:33
UC002N	NGC 3516	<i>C, K</i>	27, 230	J1048+7143	1.64	Jul-30 16:38 – Jul-31 02:44
UC002O	NGC 1068	<i>K</i>	230	J0239–0234	2.72	Aug-5 08:47 – Aug-5 16:40
UC002P	NGC 1068	<i>L, C, X</i>	55, 27, 62	J0239–0234	2.72	Aug-6 09:41 – Aug-6 15:45
UC002Q	NGC 2110	<i>K</i>	230	J0553–0840	1.27	Aug-28 10:26 – Aug-28 18:10
UC002R	NGC 2110	<i>L, C, X</i>	54, 27, 62	J0553–0840	1.27	Aug-29 11:36 – Aug-29 17:35
UC002T	NGC 2992	<i>K</i>	230	J0941–1335	1.34	Oct-17 10:57 – Oct-17 18:55
UC002U	NGC 2992	<i>L, C, X</i>	54, 27, 62	J0941–1335	1.34	Oct-19 11:49 – Oct-19 17:48
UC002W	NGC 4235	<i>L, C, X</i>	54, 27, 62	J1214+0829	1.40	Dec-23 10:28 – Dec-23 16:28
UC002X	NGC 4235	<i>K</i>	230	J1214+0829	1.40	Dec-17 09:32 – Dec-17 17:30
Obs. Date Range (2022)						
UC002Y	NGC 4593	<i>K</i>	230	J1248–0632	2.48	Jan-6 08:38 – Jan-6 16:37
UC002Z	NGC 4593	<i>L, C, X</i>	54, 27, 62	J1248–0632	2.48	Jan-4 09:46 – Jan-4 15:49
UC002AA <sup>a</sup>	NGC 3079	<i>K</i>	288	J0957+5522	0.68	Aug-31 13:33 – Aug-31 23:23
UC002AB <sup>a</sup>	NGC 4388	<i>K</i>	230	J1225+1253	0.28	Oct-18 13:29 – Oct-18 21:12
UC002AC <sup>a</sup>	NGC 5506	<i>K</i>	230	J1411–0300	0.58	Oct-3 16:23 – Oct-4 00:12
UC002AD <sup>a</sup>	NGC 3516	<i>L, X</i>	55, 62	J1048+7143	1.64	Aug-4 20:48 – Aug-5 00:51

**Note.** The rest frequencies for the *L, C, X*, and *K* bands are 1.376, 4.112, 8.376, and 21.712 GHz, respectively. The phase calibrator sources were taken from the ICRF3 S/X catalog (Charlot et al. 2020) and the Radio Fundamental Catalog (<http://astrogeo.smce.nasa.gov/rfc/>; only for J1014+5503 and J1411–300).

<sup>a</sup> VLBA follow-up observation segments.

densities can provide a meaningful comparison in SED fitting. In the following, we summarize the specific details of the source images and SED plots. We have also added the coordinates obtained from our phase-referenced VLBA measurements, with precision truncated to the formal uncertainties in the phase reference source catalogs (please see Table 2).

NGC 1052 [ $2^{\text{h}}41^{\text{m}}04^{\text{s}}.7985$ ,  $-08^{\circ}15'20''.751$ ]. All four band images revealed a bright center with extended east–west double-sided collimated outflows. Similar double-sided outflows have been observed in multiple previous VLBA studies of this source (Kamen et al. 2003; Sawada-Satoh et al. 2008; Baczko et al. 2022). NGC 1052 is the only source in our sample showing a prominent double-sided jet-like collimated structure extending outward from the central region, even with the high-resolution ( $\leq 1$  pc) *K*-band observation. The four-frequency SED plot shows a gigahertz-peaked (curved) spectrum with a peak near  $\sim 5$  GHz. The piecewise regression model yields two different spectral slopes ( $\alpha$ ) with two linear functions connected to a “knot value,” indicating steep spectral indices at high frequencies and an inverted spectral slope at

lower frequencies. The two additional SED subplots using only the *C* and *X* bands show similar spectral shapes, which indicates that the bright central region has a compact point-like structure.

NGC 1068 [ $2^{\text{h}}42^{\text{m}}40^{\text{s}}.70890$ ,  $00^{\circ}00'48''.0062$ ]. This source is detected in the *C* and *X* bands, but not in *L* and *K*. Note that NGC 1068 suffers from severe short spacing issues, due to the bright, extended radio continuum emission, and that the nondetection at the *L* band may be due to these effects. However, all four band peak intensities, including the  $5\sigma$  nondetection upper limits, show a flat (typically, if  $\alpha > -0.5$ ) spectrum. A little extended structure was detected in the *C*-band image; as a result, a steeper spectrum was seen when  $\alpha$  was measured only between the *C*- and *X*-band integrated flux densities.

NGC 2110 [ $5^{\text{h}}52^{\text{m}}11^{\text{s}}.3763$ ,  $-07^{\circ}27'22''.519$ ]. The *L*-, *C*-, and *X*-band images revealed a bright point source at the center. No emission was detected in the *K*-band image, so we used the nondetection upper limit for the SED. A gigahertz-peaked spectrum (GPS) is found for NGC 2110, with a steeper spectrum in the higher-frequency regime beyond  $\sim 5$  GHz. The



**Table 3**  
Radio Image Properties

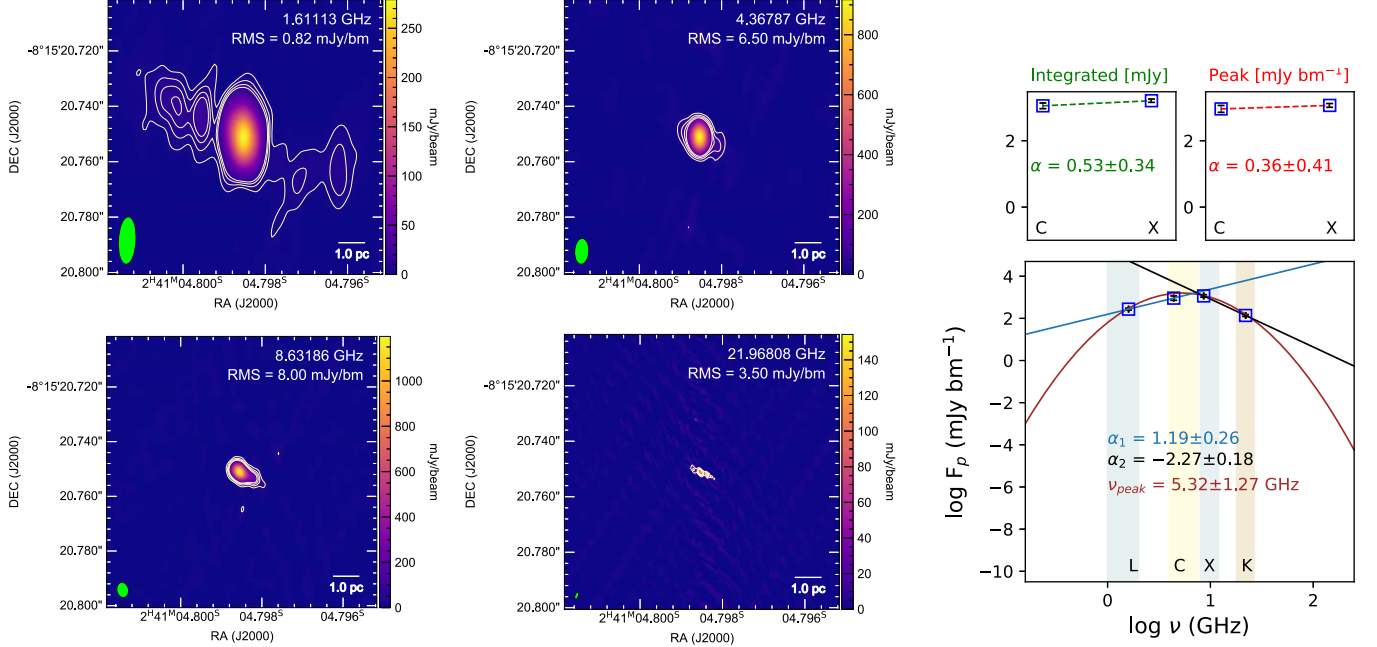
Target	Frequency Band	Restoring Beam ( $\alpha \times \delta$ ; mas)	Beam Angle (deg)	RMS (mJy $\text{bm}^{-1}$ )	$F_{\text{Gauss}}^{\text{peak}}$ (mJy $\text{bm}^{-1}$ )	$S_{\text{Gauss}}^{\text{int}}$ (mJy)	Self-calibration Applied
NGC 1052	<i>L</i>	$16.32 \times 5.53$	−3.05	0.82	$273.5 \pm 1.2$	$461 \pm 8$	Yes
	<i>C</i>	$8.53 \times 4.25$	−3.25	6.50	$912 \pm 15$	$1131 \pm 30$	Yes
	<i>X</i>	$4.76 \times 3.42$	10.81	8.00	$1162 \pm 47$	$1610 \pm 100$	Yes
	<i>K</i>	$1.62 \times 0.38$	−20.15	3.50	$137.2 \pm 6.9$	$636 \pm 44$	Yes
NGC 1068	<i>L</i>	$19.04 \times 9.12$	−0.73	0.11	<0.55	...	...
	<i>C</i>	$7.64 \times 4.27$	−5.53	0.05	$0.72 \pm 0.06$	$2.60 \pm 0.28$	No
	<i>X</i>	$4.18 \times 3.16$	−0.60	0.04	$0.37 \pm 0.02$	$0.39 \pm 0.04$	No
	<i>K</i>	$1.02 \times 0.32$	−13.64	0.04	<0.20	...	...
NGC 2110	<i>L</i>	$13.63 \times 4.84$	−9.79	0.16	$4.53 \pm 0.15$	$12.17 \pm 0.62$	No
	<i>C</i>	$8.25 \times 4.40$	2.63	0.12	$40.81 \pm 0.37$	$42.76 \pm 0.70$	Yes
	<i>X</i>	$5.01 \times 3.34$	3.05	0.06	$29.07 \pm 0.17$	$35.48 \pm 0.34$	Yes
	<i>K</i>	$1.33 \times 0.34$	−14.44	0.05	<0.25	...	...
NGC 2992	<i>L</i>	$14.84 \times 4.96$	−7.61	0.09	$2.04 \pm 0.13$	$3.81 \pm 0.40$	No
	<i>C</i>	$8.63 \times 4.10$	3.22	0.10	$1.78 \pm 0.07$	$1.83 \pm 0.13$	No
	<i>X</i>	$5.18 \times 3.01$	3.72	0.10	$1.56 \pm 0.10$	$1.37 \pm 0.17$	No
	<i>K</i>	$1.69 \times 0.42$	−16.29	0.09	$0.62 \pm 0.05$	$0.74 \pm 0.15$	No
NGC 3079	<i>L</i>	$9.81 \times 4.95$	−11	0.25	$6.33 \pm 0.27$ (A) <1.25 (B)	$9.5 \pm 0.7$ (A) ...(B)	Yes Yes
	<i>C</i>	$5.13 \times 4.15$	8.53	0.13	$53.10 \pm 0.85$ (A)	$85.1 \pm 2.0$ (A)	Yes
					$11.31 \pm 0.10$ (B)	$13.27 \pm 0.19$ (B)	Yes
	<i>X</i>	$3.59 \times 3.12$	17.12	0.16	$22.92 \pm 0.75$ (A) $28.32 \pm 0.56$ (B)	$47.9 \pm 2.2$ (A) $35.2 \pm 1.1$ (B)	Yes Yes
NGC 3516	<i>K</i>	$0.55 \times 0.39$	−18.8	0.06	<0.30 (A) ...<0.30 (B)	...(A) ...(B)	... ...
	<i>L</i>	$10.28 \times 4.71$	−17.07	0.11	$2.09 \pm 0.16$	$3.26 \pm 0.47$	Yes
	<i>C</i>	$5.29 \times 4.77$	−3.22	0.04	$0.52 \pm 0.03$	$0.72 \pm 0.07$	No
	<i>X</i>	$3.52 \times 2.66$	−5.31	0.05	$0.49 \pm 0.02$	$0.82 \pm 0.06$	No
NGC 4151	<i>K</i>	$2.11 \times 1.81$	25.33	0.09	<0.45	...	...
	<i>L</i>	$11.64 \times 5.64$	−7.08	0.09	$8.02 \pm 0.53$	$24.7 \pm 2.0$	Yes
	<i>C</i>	$5.53 \times 4.07$	−13.81	0.07	$8.77 \pm 0.56$	$28.3 \pm 2.3$	Yes
	<i>X</i>	$3.72 \times 3.50$	37.38	0.12	$4.84 \pm 0.29$	$21.7 \pm 1.6$	Yes
NGC 4235	<i>K</i>	$1.97 \times 0.86$	43.37	0.06	$0.27 \pm 0.03$	$0.79 \pm 0.18$	No
	<i>L</i>	$12.99 \times 4.98$	−10.68	0.06	$1.43 \pm 0.07$	$1.81 \pm 0.16$	No
	<i>C</i>	$9.34 \times 5.24$	42.02	0.13	$3.06 \pm 0.15$	$3.21 \pm 0.28$	No
	<i>X</i>	$4.83 \times 3.49$	41.99	0.11	$1.97 \pm 0.10$	$3.59 \pm 0.28$	No
NGC 4388	<i>K</i>	$2.37 \times 1.35$	21.18	0.09	<0.45	...	...
	<i>L</i>	$14.40 \times 4.39$	−15.57	0.03	$0.19 \pm 0.02$	$0.22 \pm 0.05$	No
	<i>C</i>	$8.65 \times 4.19$	−19.22	0.04	$0.23 \pm 0.02$	$0.59 \pm 0.08$	No
	<i>X</i>	$3.94 \times 3.28$	1.81	0.05	$0.25 \pm 0.02$	$0.41 \pm 0.06$	No
NGC 4593	<i>K</i>	$1.27 \times 0.53$	−11.14	0.08	<0.40	...	...
	<i>L</i>	$15.30 \times 5.17$	−7.01	0.06	<0.30	...	...
	<i>C</i>	$7.90 \times 4.36$	27.39	0.06	$0.65 \pm 0.04$	$0.77 \pm 0.08$	No
	<i>X</i>	$5.58 \times 3.88$	31.37	0.05	$0.47 \pm 0.05$	$0.88 \pm 0.14$	No
NGC 5290	<i>K</i>	$2.30 \times 0.53$	−14.13	0.04	$0.29 \pm 0.03$	$0.64 \pm 0.11$	No
	<i>L</i>	$9.73 \times 4.60$	9.97	0.03	$0.29 \pm 0.05$	$0.66 \pm 0.14$	No
	<i>C</i>	$4.82 \times 3.64$	−3.97	0.03	$4.75 \pm 0.02$	$4.83 \pm 0.04$	Yes
	<i>X</i>	$3.88 \times 3.34$	19.61	0.06	$6.33 \pm 0.07$	$6.74 \pm 0.13$	Yes
NGC 5506	<i>K</i>	$0.71 \times 0.38$	−7.60	0.04	$0.49 \pm 0.05$	$1.62 \pm 0.33$	No
	<i>L</i>	$16.12 \times 5.36$	−11.79	0.35	$24.3 \pm 1.5$ (B0) $8.95 \pm 0.38$ (B1)	$33.5 \pm 3.7$ (B0) $31.1 \pm 3.2$ (B1)	Yes Yes
	<i>C</i>	$7.70 \times 4.36$	6.74	0.21	$44.27 \pm 0.39$ (B0)	$48.83 \pm 0.76$ (B0)	Yes
					$6.75 \pm 0.34$ (B1)	$28.6 \pm 1.8$ (B1)	Yes
NGC 5506	<i>X</i>	$4.60 \times 3.23$	0.15	0.12	$27.43 \pm 0.26$ (B0) $1.13 \pm 0.07$ (B1)	$34.79 \pm 0.54$ (B0) $9.13 \pm 0.63$ (B1)	Yes Yes
	<i>K</i>	$1.51 \times 0.26$	−22.52	0.21	<1.05 (B0)	...(B0)	...
					<1.05 (B1)	...(B1)	...

**Note.** Peak intensities ( $F_{\text{Gauss}}^{\text{peak}}$ ) and integrated flux densities ( $S_{\text{Gauss}}^{\text{int}}$ ) are measured from CASA's 2D Gaussian model fitting algorithm. For nondetections, upper limits were measured using a  $5\sigma$  intensity limit above the rms. The beam angle is the beam's major axis position angle measured from north toward the east.

C–X-band SED subplots are similar, with much flatter indices ( $\alpha > -0.5$ ) for peak intensities and integrated flux densities, suggesting a central point source.

NGC 2992 [ $9^{\text{h}}45^{\text{m}}41^{\text{s}}.94437$ ,  $-14^{\circ}19'34''.599$ ]. NGC 2992 is detected in all four bands and shows a bright, compact radio emission at the center. The point-like nature of this source can

## NGC 1052



## NGC 1068

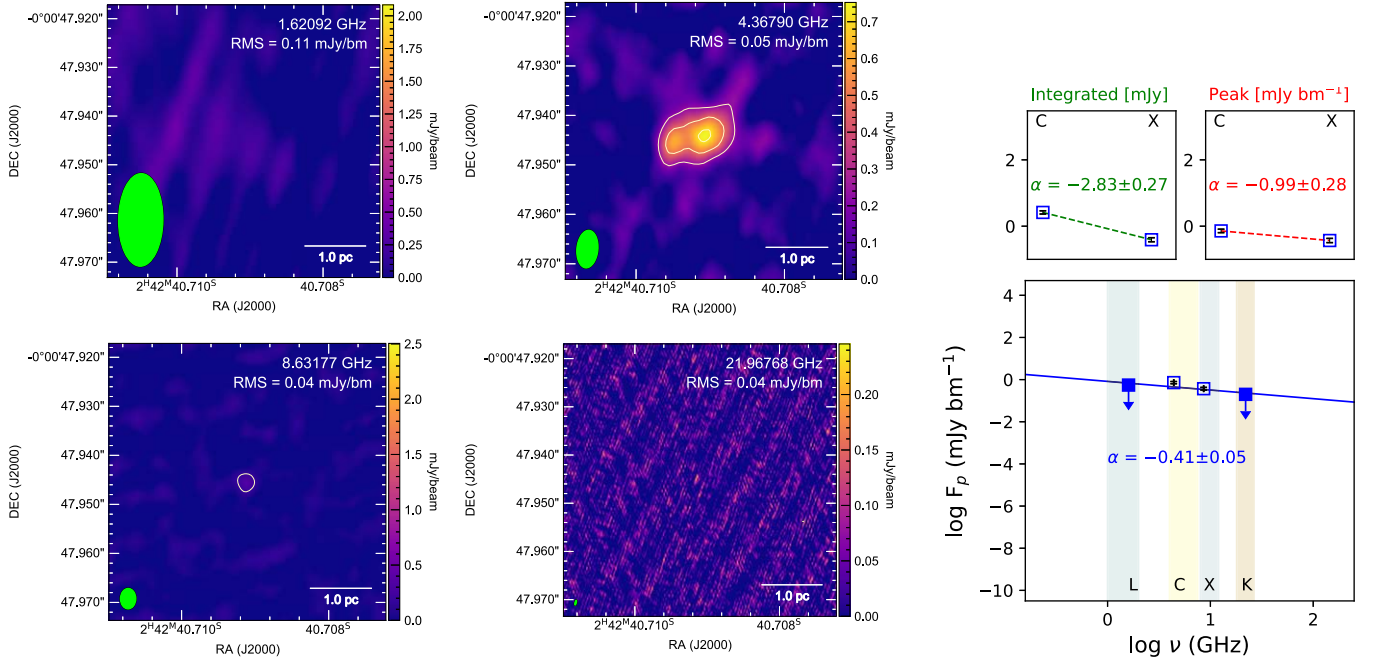


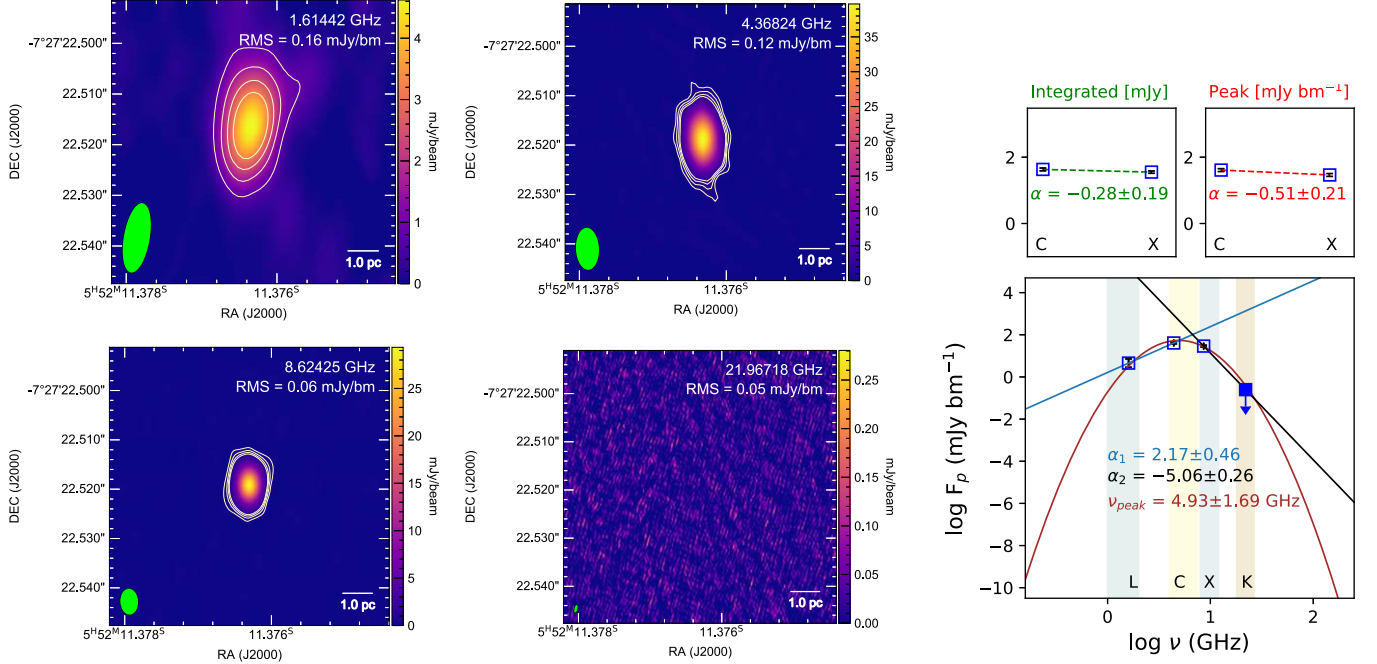
**Figure 2.** Multiband (1.6–22 GHz) parsec-scale VLBA radio observations. The outermost contour represents the  $5\sigma$  flux limit above the rms, and the interior contours increase as  $\sigma \times (10, 15, 20)$ . The green ellipses to the lower left of each frame represent the synthesized beam size for that observation. The right panel represents the SED for each source using the peak intensities of each frequency image. The nondetection upper limits ( $5\sigma$ ) are denoted by the downward arrows. The two plots in the upper panel represent the spectral shape only between 4.4 GHz (C band) and 8.6 GHz (X band) after applying UVTAPER on both images.

also be deduced from the C- to X-band flat SEDs, using both peak intensities and integrated flux densities. In addition, the four-frequency SED plot shows a flat spectrum with a spectral index  $\alpha > -0.5$ .

NGC 3079 [10<sup>h</sup>01<sup>m</sup>57<sup>s</sup>804, +55°40′47″239]. NGC 3079 is one of the two sources in our sample with multicomponent (A and B; mentioned in Trotter et al. 1998) radio sources. In addition, a third component lying between A and B was

tentatively identified in the C and X bands, but its characteristics were not well constrained by the observation. Source A was detected in the L, C, and X bands, whereas component B was seen only in the C and X bands. Including nondetection upper limits ( $5\sigma$ ), both components showed a GPS and slightly resolved point-like structures. Component A showed a turnover peak at 4.46 GHz and B showed a turnover peak at 5.60 GHz. After the turnover frequency, both components showed

## NGC 2110



## NGC 2992

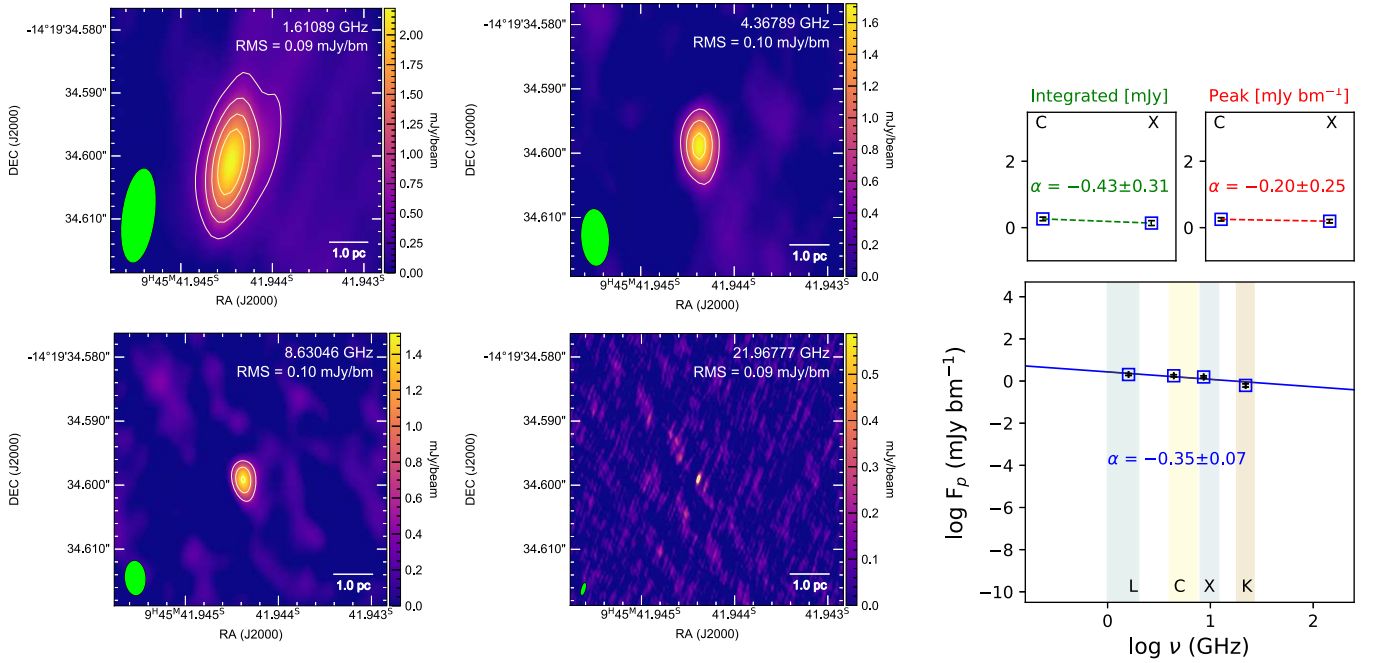


Figure 2. (Continued.)

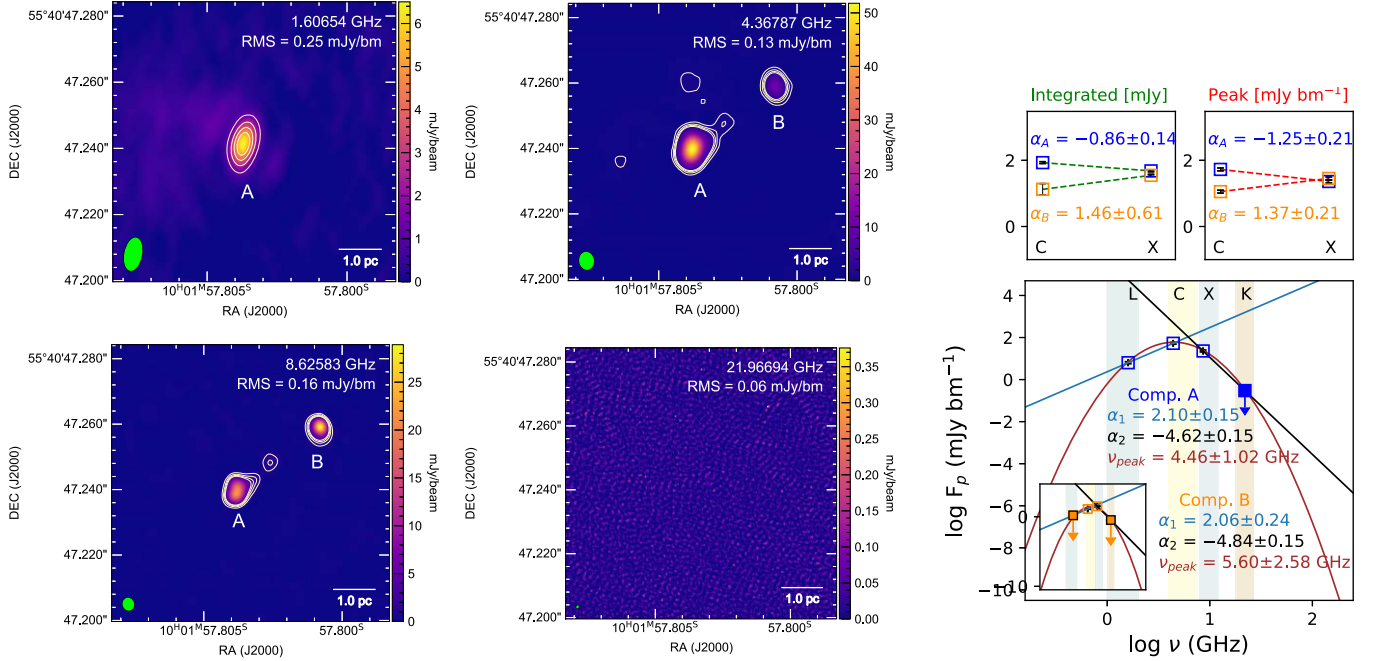
comparatively steeper spectra at high frequencies. Component A's turnover frequency is lower than B's, so component A showed a decrement of peak intensity starting near the C band. In contrast, component B's peak intensity values keep rising until the X band (as the turnover peaks at a higher frequency), with an inverted spectrum, then drop steeply at higher frequencies. This difference is also seen in the two additional SED plots using only the C- and X-band peak intensities and integrated flux densities.

NGC 3516 [11<sup>h</sup>06<sup>m</sup>47<sup>s</sup>.46352, +72°34'07".2784]. A flat spectrum ( $\alpha > -0.5$ ) was found for NGC 3516, with L-, C-, and X-band detections and the K-band upper limit. The SEDs from the peak intensities and integrated flux densities in the C and X bands show flat spectra and suggest a point source.

NGC 4151 [12<sup>h</sup>10<sup>m</sup>32<sup>s</sup>.58201, +39°24'21".063] All four band images revealed a bright, central subparsec-scale emission with a “candle flame” shape outflow in the northeast direction. The elongated structure is visible in all four band images, even



## NGC 3079



## NGC 3516

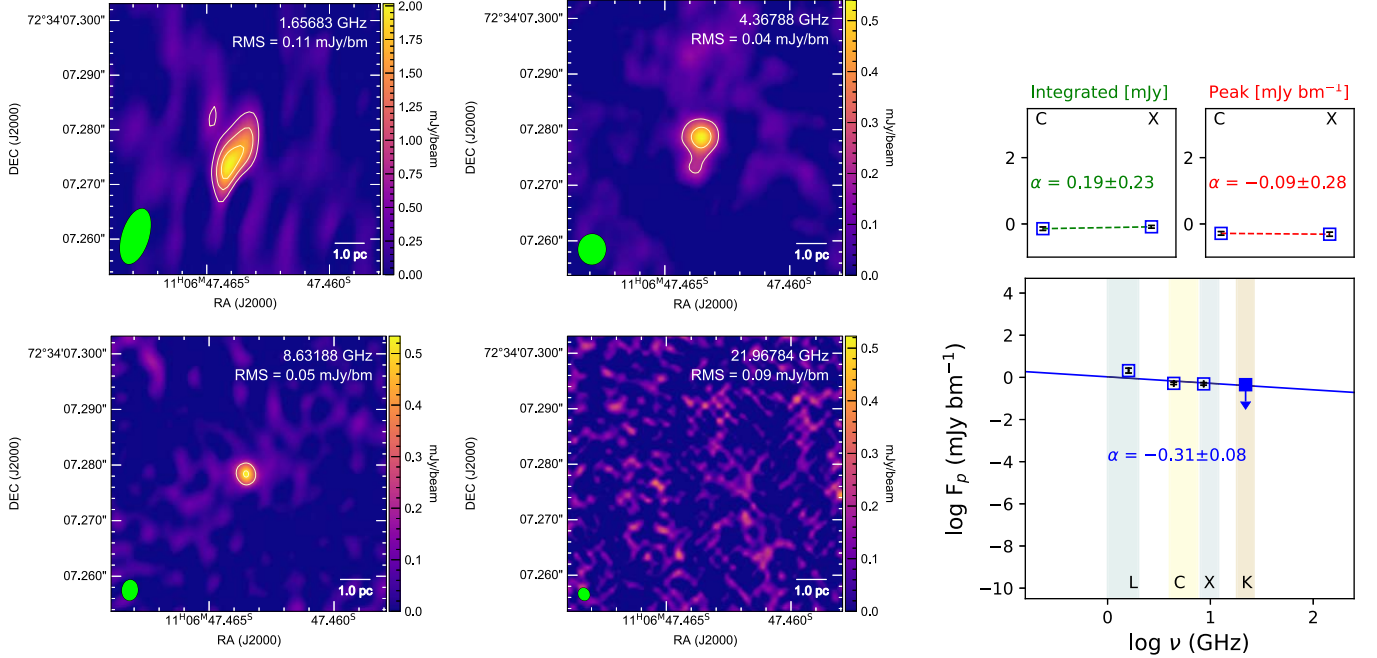


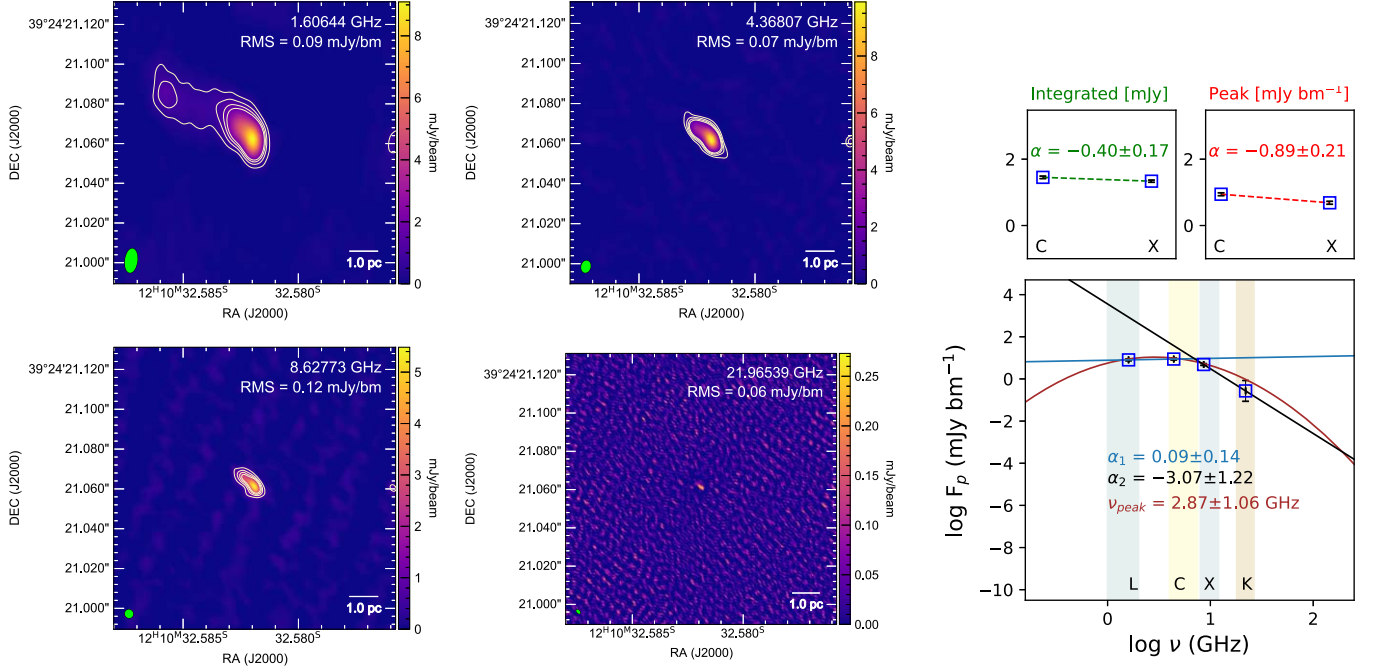
Figure 2. (Continued.)

in the high-resolution,  $K$ -band subparsec ( $\sim 0.1$  pc) spatial scale. The interesting jet/outflow structures of NGC 4151 were previously reported in various subparsec-to-parsec-scale VLBI and eMERLIN studies (Ulvestad et al. 2005; Williams et al. 2017, 2020). While plotting SEDs using only the C- and X-band peak intensities and integrated flux densities, we found flat to slightly steeper spectra, suggesting that the central region is a compact point source. The four-frequency SED model using all peak intensities showed a GPS, with a flatter spectrum

in the lower-frequency regime and a steeper spectrum at higher frequency, as the  $K$ -band peak emission is relatively weak.

NGC 4235 [ $12^{\text{h}}17^{\text{m}}09^{\text{s}}.88175$ ,  $+07^{\circ}11'29''.670$ ]. The  $L$ -,  $C$ -, and  $X$ -band images showed a point-like structure, with a little extended feature in the  $X$ -band image; thus, the integrated flux density in the  $X$  band is a little higher compared to the  $C$ -band flux density. NGC 4235 is another example of our sample with a GPS found in the four-frequency SED with a turnover frequency of about  $\sim 4.3$  GHz. The higher-frequency spectrum,

## NGC 4151



## NGC 4235

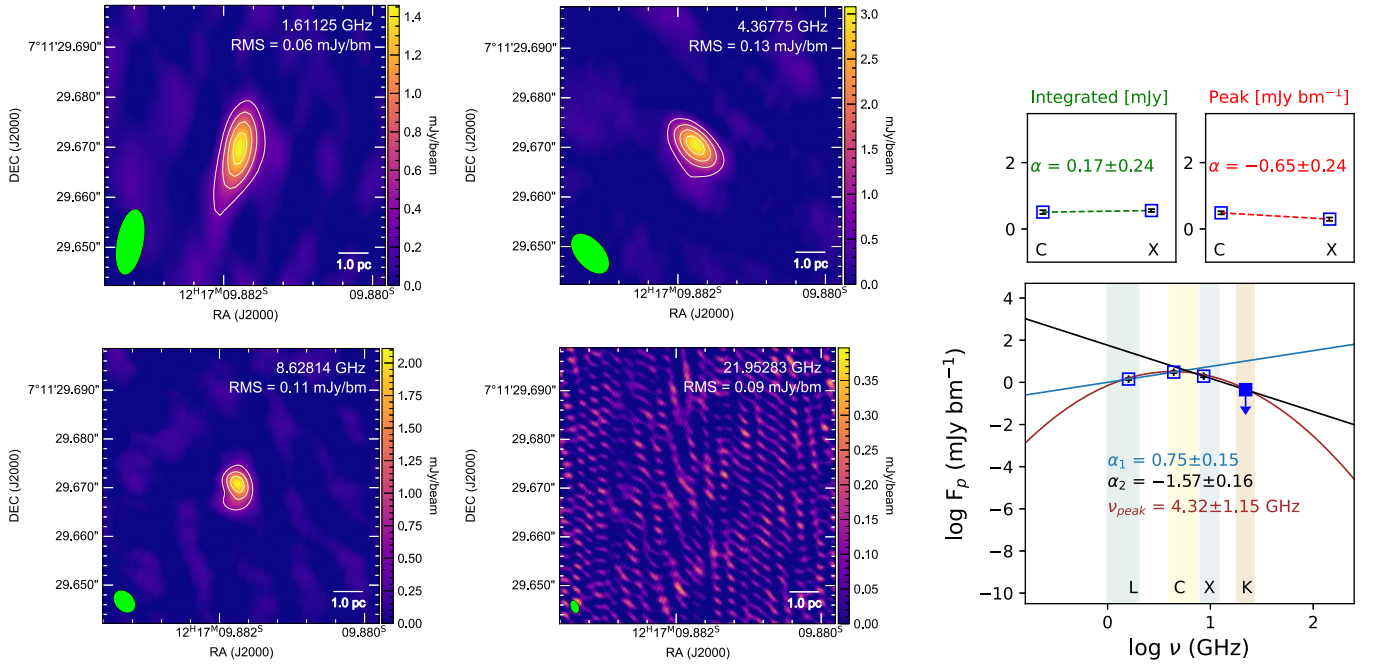


Figure 2. (Continued.)

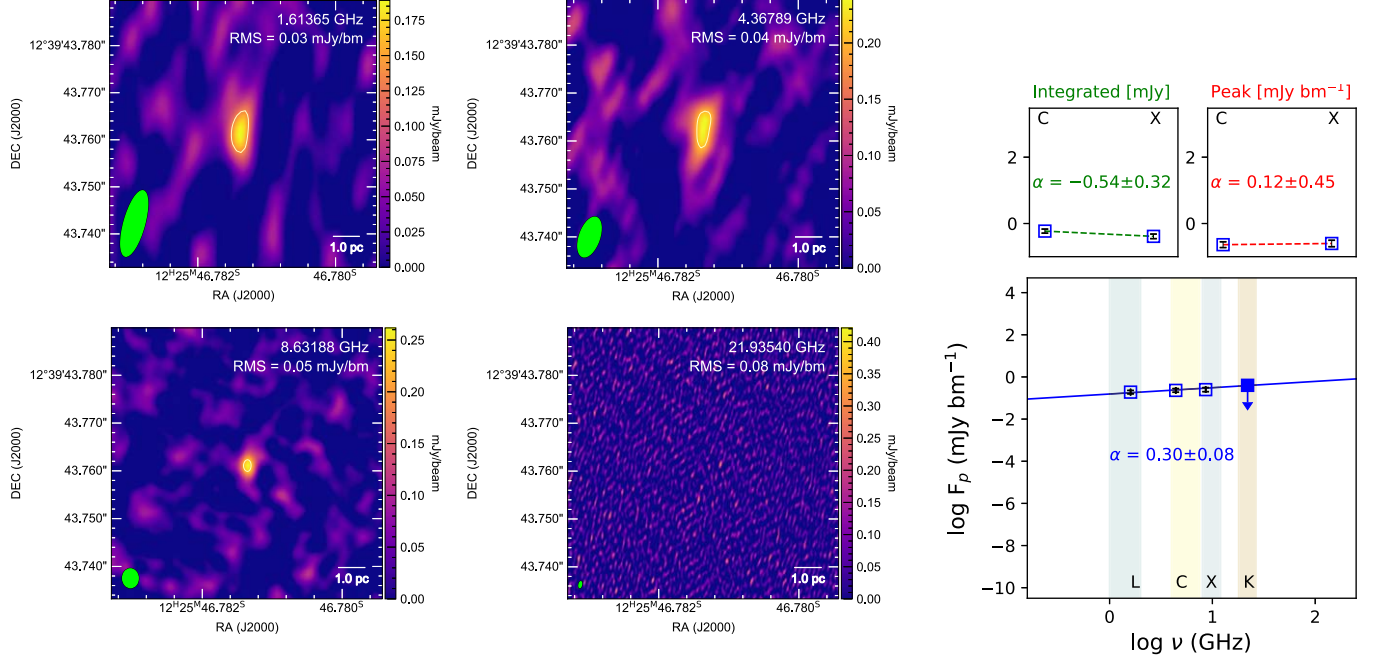
including the  $5\sigma$  nondetection upper limit in the  $K$  band, showed a steeper spectral index ( $\alpha \approx -1.6$ ).

NGC 4388 [ $12^{\text{h}}25^{\text{m}}46^{\text{s}}.78135$ ,  $+12^{\circ}39'43''.761$ ]. All four band images revealed a weak central radio emission. NGC 4388 is the weakest of all radio sources detected in the  $L$ ,  $C$ , and  $X$  bands. No  $K$ -band emission was detected. The four-frequency SED plot with the  $K$ -band upper limit shows an inverted spectrum with a spectral index of  $\sim 0.3$ .

NGC 4593 [ $12^{\text{h}}39^{\text{m}}39^{\text{s}}.44359$ ,  $-05^{\circ}20'39''.035$ ]. Similar to NGC 4388, the images reveal a weak compact core-like emission at the center. The four-frequency SED plot shows a flat spectrum with  $\alpha = 0.08$  with the  $L$ -band upper limit.

NGC 5290 [ $13^{\text{h}}45^{\text{m}}19^{\text{s}}.16076$ ,  $+41^{\circ}42'44''.463$ ]. All four band images show a bright point source at the center. The SED subplots using only the  $C$  and  $X$  bands show a similar flat spectrum, supporting the idea of a point source. The four-

## NGC 4388



## NGC 4593

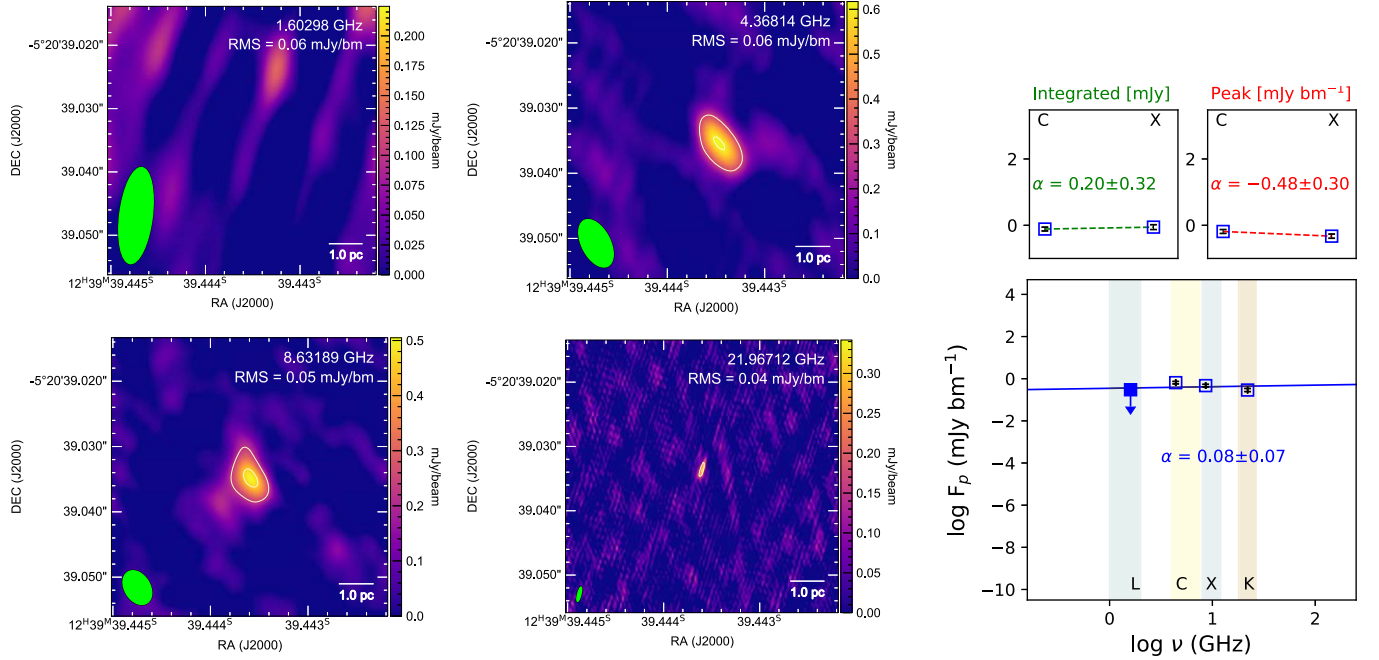


Figure 2. (Continued.)

frequency SED plot shows a GPS with a peak at 6.70 GHz. A similar radio peak intensity drop was seen at the lower- and higher-frequency ends.

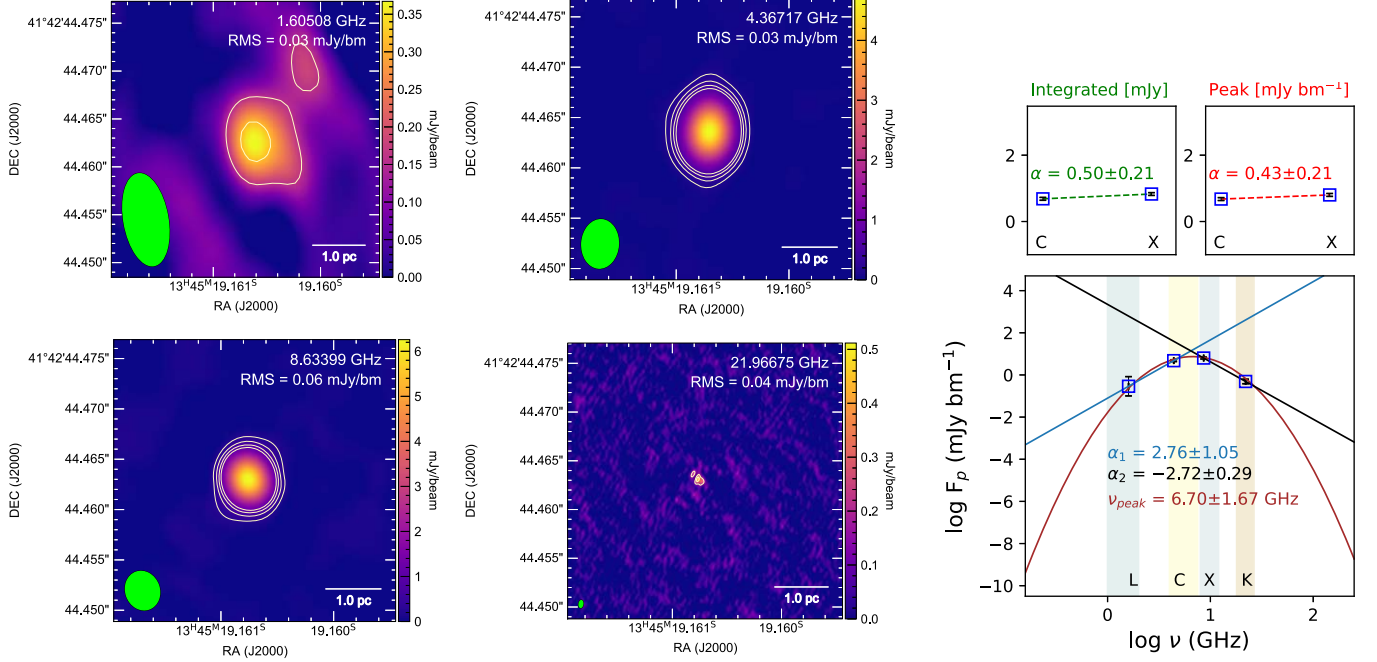
NGC 5506 [ $14^{\text{h}}13^{\text{m}}14^{\text{s}}87735$ ,  $-03^{\circ}12'27''.6585$ ]. We detected two components (B0 and B1; mentioned in Middelberg et al. 2004) in the  $L$ -,  $C$ -, and  $X$ -band images. Neither component was detected in the  $K$  band. All three detected images and the central two-frequency ( $C$ - and  $X$ -band) SEDs using peak intensities and integrated flux densities suggested a

pair of two point-like sources slightly resolved in the  $C$  band. But their four-frequency SED plot shows that component B0 follows a GPS with a turnover peak near  $\sim 4$  GHz, whereas the component B1 peak intensities dropped with the frequency increase, resulting in a steeper spectrum.

Table 4 lists all our sources' spectral shapes and indices, including turnover frequencies from the GPS, lower- and higher-frequency-domain spectral indices ( $\alpha_1$  and  $\alpha_2$ ), and



## NGC 5290



## NGC 5506

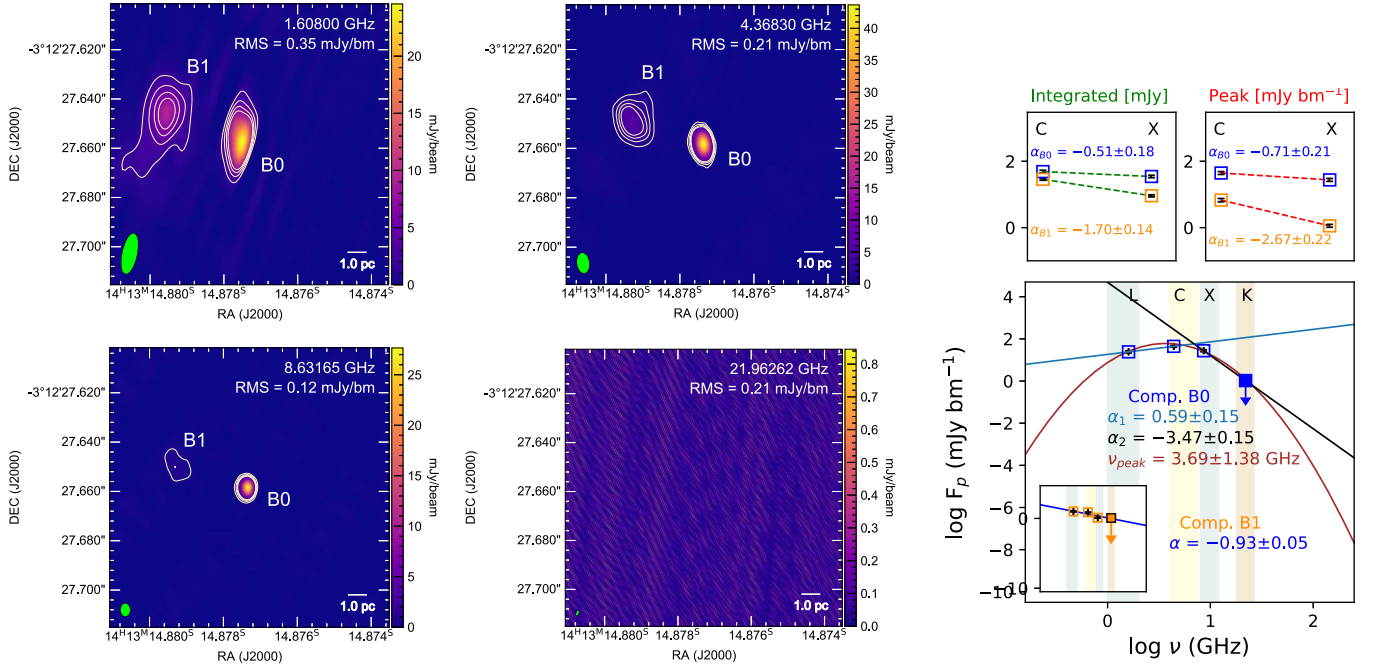


Figure 2. (Continued.)

spectral indices derived from the C- and X-band peak intensities and integrated flux densities only ( $\alpha^{\text{int}}$  and  $\alpha^{\text{peak}}$ ).

#### 4. Discussion

##### 4.1. Detection Rate and Central Radio Emission

In FRAMEx Papers I and III, with the help of VLBA subparsec-scale ( $\sim$ milliarcsecond resolution) observations in the C (5.8 GHz) band, the detection fraction was  $\sim 33\%$ – $36\%$ ,

in contrast with lower-resolution kiloparsec-scale VLA (archival) observations ( $\sim$ arcsec resolution), taken in A configurations at  $\sim 4.89$  GHz, where the detection fraction was about  $\sim 100\%$ . We suggested that the high detection fraction in the kiloparsec scale was due to the extranuclear radio emission from interactions between the AGN and the host environment. Now, in this work, we have observed 12 detected sources from Papers I and III in the L (1.6 GHz), C (4.4 GHz), X (8.6 GHz), and K (22 GHz) bands using VLBA with a sensitivity depth of

**Table 4**  
Radio Spectral Index

Gigahertz-peaked	$\nu_{\text{peak}}$ (1)	$\alpha_1$ (2)	$\alpha_2$ (3)	$\alpha_{(4.4-8.6)}^{\text{int}}$ (4)	$\alpha_{(4.4-8.6)}^{\text{peak}}$ (5)
NGC 1052	$5.32 \pm 1.27$	$1.19 \pm 0.26$	$-2.27 \pm 0.18$	$0.36 \pm 0.41$	$0.53 \pm 0.34$
NGC 2110	$4.93 \pm 1.69$	$2.17 \pm 0.46$	$-5.06 \pm 0.26$	$-0.28 \pm 0.19$	$-0.51 \pm 0.21$
NGC 3079 (A)	$4.46 \pm 1.02$	$2.10 \pm 0.15$	$-4.62 \pm 0.15$	$-0.86 \pm 0.14$	$-1.25 \pm 0.21$
NGC 3079 (B)	$5.60 \pm 2.58$	$2.06 \pm 0.24$	$-4.84 \pm 0.15$	$1.46 \pm 0.61$	$1.37 \pm 0.21$
NGC 4151	$2.87 \pm 1.06$	$0.09 \pm 0.14$	$-3.07 \pm 1.22$	$-0.40 \pm 0.17$	$-0.89 \pm 0.21$
NGC 4235	$4.32 \pm 1.15$	$0.75 \pm 0.15$	$-1.57 \pm 0.16$	$0.17 \pm 0.24$	$-0.65 \pm 0.24$
NGC 5290	$6.43 \pm 1.32$	$2.76 \pm 0.28$	$-2.72 \pm 0.22$	$0.50 \pm 0.21$	$0.43 \pm 0.21$
NGC 5506 (B0)	$3.69 \pm 1.38$	$0.59 \pm 0.15$	$-3.47 \pm 0.15$	$-0.51 \pm 0.18$	$-0.71 \pm 0.21$
Steep/flat /inverted		$\alpha_{(1.6-22)}$ (6)		...	...
NGC 1068		$-0.41 \pm 0.05$		$-2.83 \pm 0.27$	$-0.99 \pm 0.28$
NGC 2992		$-0.35 \pm 0.07$		$-0.43 \pm 0.31$	$-0.20 \pm 0.25$
NGC 3516		$-0.31 \pm 0.08$		$0.19 \pm 0.23$	$-0.09 \pm 0.28$
NGC 4388		$0.30 \pm 0.08$		$-0.54 \pm 0.32$	$0.12 \pm 0.45$
NGC 4593		$0.08 \pm 0.07$		$0.20 \pm 0.32$	$-0.48 \pm 0.30$
NGC 5506 (B1)		$-0.93 \pm 0.05$		$-1.70 \pm 0.14$	$-2.67 \pm 0.22$

**Notes.** Column (1): turnover frequency from best-fitting quadratic polynomial function. Columns (2) and (3):  $\alpha_1$  and  $\alpha_2$  were measured using a piecewise linear regression fit for the sources with a GPS. Columns (4) and (5):  $\alpha_{(4.4-8.6)}^{\text{int}}$  and  $\alpha_{(4.4-8.6)}^{\text{peak}}$  were measured between 4.4 and 8.6 GHz using their respective peak intensities and integrated flux densities derived from CASA's 2D Gaussian model fitting algorithm. Column (6):  $\alpha_{(1.6-22)}$  values were measured for the sources with a single power-law spectrum between 1.6 and 22 GHz.

$\sim 25 \mu\text{Jy bm}^{-1}$  per band to probe the actual origin of radio emission in the subparsec regime.

We detected 12 out of 12 of our sources in the *C* and *X* bands, whereas 10 out of 12 ( $\sim 83\%$ ) sources were detected in the *L* band and 5 out of 12 ( $\sim 42\%$ ) sources were detected in the *K* band. We found a relatively higher detection rate than previous high-resolution (VLBA and eMERLIN) studies at low frequency (*L* band/1.6 GHz). For example, in a study of 103 nearby galaxies from the Palomar sample observed at 1.5 GHz with the high-resolution ( $\sim 150$  mas) eMERLIN array, they found a  $\sim 50\%$  detection rate (Baldi et al. 2018). A similar fraction of detection was reported in a VLBA study of a sample of RL and RQ AGNs at 1.4 GHz in Maini et al. (2016). In addition, all these studies found that most detected sources are either single radio core detections or sometimes associated with more complex structures similar to ours. The VLBA detected subparsec-scale emission at 1.6 GHz in 83% of our targets. In FRAMEX Paper III, we showed that synchrotron self-absorption could cause low detection rates at VLBA spatial scales at *C*-band frequencies. Thus, at the *L* band, one would infer these effects to be more prominent, as synchrotron self-absorption is even more dominant at 1.6 GHz than at 5–6 GHz.

At the higher end of the spectrum, we found  $\sim 42\%$  detection with the VLBA in the *K* band. In contrast, in a JVLA study of 100 ultrahard-X-ray-selected AGNs at *K* band (22 GHz), Smith et al. (2020) detected 96% of their sample. They found a compact radio core detection for all sources. But their comparatively low-resolution ( $\sim 1''$ ) radio study did not differentiate between synchrotron emission from AGN cores and thermal or free-free emission from dust or star formation. Though our detection fraction is not as high as this previous study, the higher-resolution observations, including the *K* band, found the radio-emitting regions within a parsec of the center engine of the AGNs. A low detection rate or lower luminosity in the *K* band at parsec scale suggests the synchrotron emission can still be detected in higher frequency (until or beyond

22 GHz) in opposition to large-scale VLA radio detections, where the thermal emission from dust can dominate in that frequency range.

Now the question that needs to be addressed is whether this central radio emission is associated with collimated outflows (for example, small-scale jets), accretion disk coronae, or interactions between the nearby interstellar medium (ISM) and small-scale AGN outflows or winds. In the next section, we investigate the different physical mechanisms at work in our sample of AGNs using subparsec-scale radio spectral index analysis.

#### 4.2. GPS

GPS is a term used to describe a type of radio source that emits radiation predominantly in the GHz frequency range, with a peak (turnover) in its SED at gigahertz frequencies (typically  $\sim 1$  GHz; de Vries et al. 1997). The turnover frequency is characterized by a change in the spectral index (the slope of the SED), from a flatter value at lower frequencies to a steeper value at higher frequencies. At lower frequencies, the radiation can be absorbed by the relativistic electrons (synchrotron self-absorption) and/or by thermal electrons (free-free absorption), causing a flat/inverted slope in the low-frequency domain. Higher-energy electrons can radiate their energy, causing steeper spectra at high frequencies. These phenomena combined create convex-shaped radio spectra with a spectral turnover frequency between hundreds of megahertz and a few gigahertz (Snellen et al. 1998; Patil et al. 2018). The physical mechanisms responsible for the GPS phenomenon are still poorly understood, but they are believed to be young, compact radio sources representing the early stages of massive RL AGNs' life cycles (Fanti et al. 1990; O'Dea et al. 1991; O'Dea 1998; Lister 2003; Sotnikova et al. 2019; Patil et al. 2020).



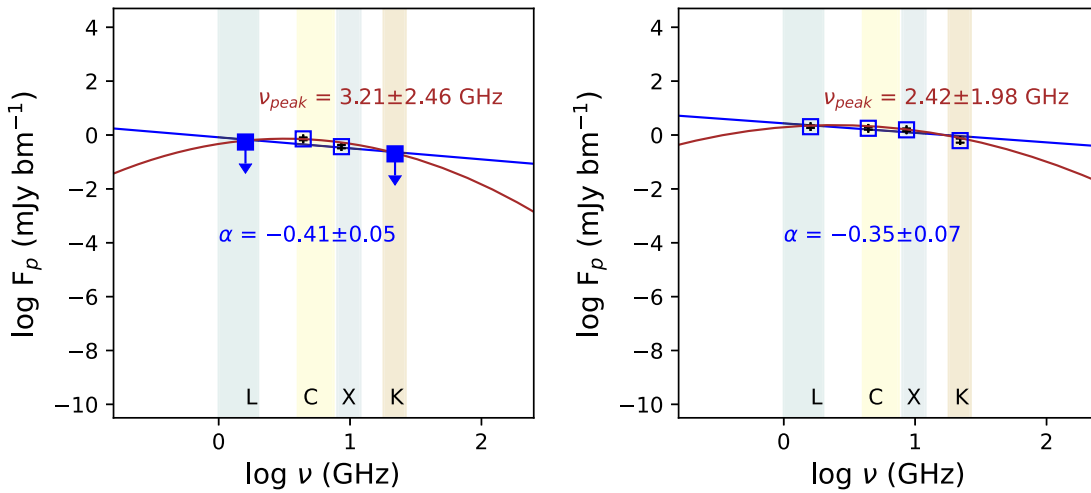


**Figure 4.** NGC 1068 (left) and NGC 2992 (right) are examples of nearly steep spectra sources or they may be peaked spectrum sources with lower turnover frequency than the other GPS sources in our sample. It is believed that lower-turnover-frequency sources might be in the transient or intermittent stage between GPS sources (a few gigahertz) to CSS sources (hundreds of megahertz).

A recent study of high-frequency, high-resolution VLBI observations of GPS sources by Cheng et al. (2023) mainly found a compact core (associated with the one-sided jet feature) and a turnover frequency ranging from 6 and 32 GHz. Similarly, our study found GPS sources (7 out of 12) mainly with a parsec- to subparsec-scale central radio-emitting region, with a few having an extended outflow-like structure (e.g., NGC 1052) and multicomponent features (e.g., NGC 3079, NGC 5506). The turnover frequencies range from  $\sim 3$  to 6 GHz (see Table 4). The turnover scenario is consistent with the idea we proposed in Paper III: free-free or self-absorbed synchrotron radiation or a combination of both can happen at lower frequencies ( $\leq 5$  GHz), where shocks accelerate relativistic electrons within the accretion flow of AGNs. In addition, a model proposed by Ishibashi & Courvoisier (2011) suggested that the opacity decreases with the frequency increase and the transition from optically thick to optically thin regimes lies at around a few tens of gigahertz. So, in the low-frequency regime for VLBA resolutions, we can expect inverted spectra due to the radiation absorbed by the relativistic electrons, which would lead to a peak near a few gigahertz.

We found an interesting linear correlation,  $\nu_p = (1.07 \pm 0.27)\alpha_1 + 3.16$ , when we plotted turnover frequencies ( $\nu_p$ ) with lower-frequency spectral indices or  $\alpha_1$  (Figure 3). This correlation means that the radio intensity drops more rapidly or, in other words, absorption is higher (free-free or synchrotron) at lower frequencies for the sources with higher turnover frequencies. Recent proper-motion studies and multi-frequency polarization observations have established that GPS sources are young objects embedded in a dense ISM and interacting with it (O’Dea & Saikia 2021). Previously, from observational studies of GPS sources, an anticorrelation was found between turnover frequency and source size (O’Dea & Baum 1997). That means the youngest objects have the highest turnover frequencies, and as the source expands and the energy density decreases, the peak frequency is expected to move toward a lower frequency (Tinti et al. 2005). These results combined established that the absorption is higher in the dense central region of young radio AGNs. As most of our sources are relatively higher-accreting AGNs (see Section 4.5), higher density is expected in their central parsec regions, representing the young radio AGN group.

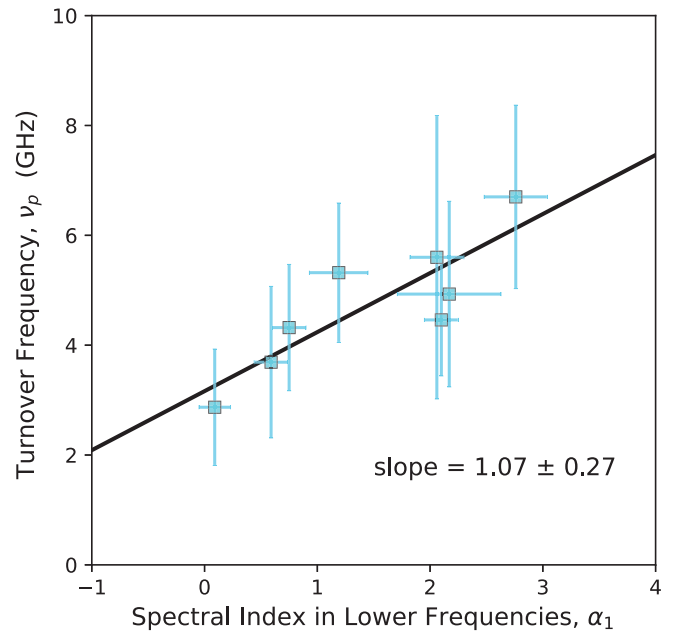


**Figure 3.** Correlation between the inverted spectral index at lower frequencies and turnover (peak) frequencies in GPS sources. The peak frequencies have large uncertainties due to the contribution of the *L*- and *K*-band nondetection upper limits.

#### 4.3. Steep, Flat, or Inverted Spectra

Hovatta et al. (2014) showed differences in the distributions of the observed spectral indices between core and jet components of AGNs from a four-frequency (8.1, 8.4, 12.1, and 15.4 GHz) VLBA observation of 190 extragalactic radio jets in the MOJAVE survey. They demonstrated that the emission with a flatter ( $\alpha > -0.5$ ) spectrum is generated in the inner part or close to the central core, and the jet spectra are relatively steeper with a mean index value  $\alpha \approx -1$ . More recently, in a (sub)kiloparsec-scale VLA study of a sample of 30 nearby (RQ) AGNs, Panessa et al. (2022) found  $\sim 70\%$  of the sources either with steep spectra ( $\alpha \leq -0.5$ ), or flat spectra ( $\alpha > -0.5$ ). They suggested that the steep spectra are compatible with optically thin synchrotron emission from a

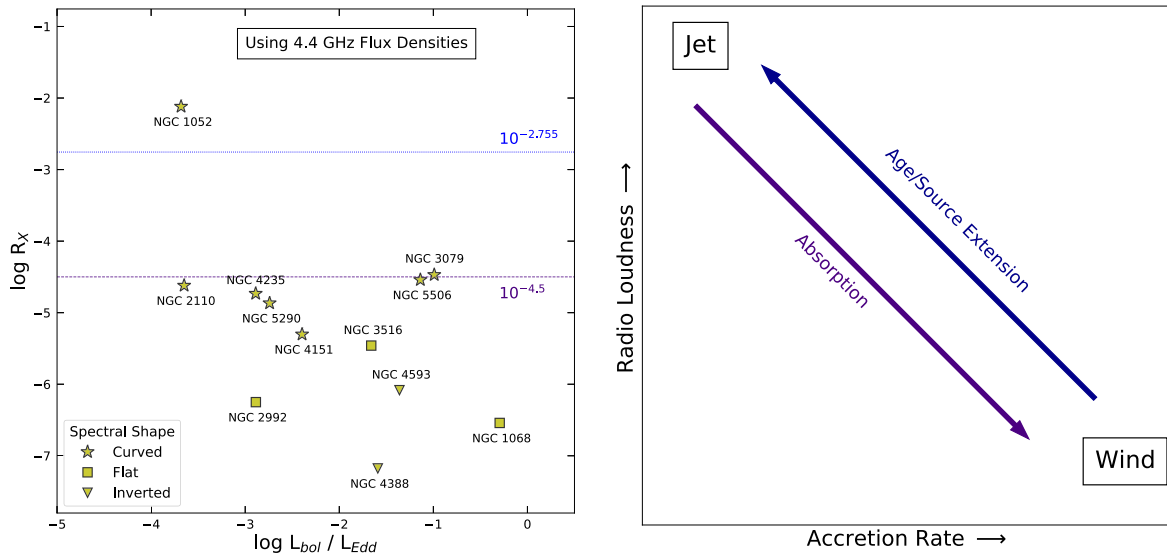


**Figure 5.** Left: radio loudness vs. Eddington ratio plot for our sample with their spectral shapes, where the radio loudness was determined using flux densities from the  $5\sigma$  contour region of our 4.4 GHz observations. The blue dotted line indicates the separation between RL and RQ AGNs, as introduced by Panessa et al. (2007), and separates Seyferts from LLRGs of  $L_R/L_X = 10^{-2.755}$ . The purple dashed line represents the classical division between RL and RQ AGNs by Terashima & Wilson (2003). The plot shows that the flat and inverted spectra are associated with the sources with higher accretion rates and lower radio luminosities. Right: a schematic diagram representing the differences in physical mechanisms responsible for radio emission as a function of absorption and source age in the same parameter space.

jet or disk winds, which are unresolved in compact cores, and flat-spectrum sources are generally compact, indicating a possible optically thick synchrotron emission from a compact jet, a hot corona, or both. They also calculated the mean of the slopes of the cores and found a nearly flat gradient ( $\alpha > -0.5$ ) had been observed from 5 to 15 GHz, which steepened sharply from 15 to 22 GHz ( $\alpha < -1.0$ ). So, optically thick core synchrotron emission was suggested below 15 GHz for their sample of relatively higher-accreting RQ AGNs, which becomes optically thin above 15 GHz. Now, if any small (parsec-scale) optically thin radio lobe/jet was the possible physical mechanism here, the slope might have been steeper in lower frequencies as well (Gültekin et al. 2022).

In principle, steeper spectra are associated with optically thin synchrotron jets (unresolved in compact cores). A flatter spectrum is associated with optically thick inner core radio emission from winds or shocks. We found the remaining 5 out of 12 sources to have nearly flat or inverted spectra ( $\alpha > -0.5$  or  $\alpha > 0$ ), and a component of NGC 5506 (B1) separated by 4–5 pc from the central B0 source showed steep spectra with  $\alpha < -0.5$  (see Table 4). Sources with flat spectra showed mostly resolved/slightly resolved bright central regions, establishing that the radio emission is from parsec-scale winds/shocks at the immediate vicinity of these AGNs. The NGC 5506 (B1) component with a steep spectrum ( $\alpha \sim -0.93$ ) may originate from a small-scale, optically thin, one-sided, strong collimated outflow or interaction with the neighboring ISM. On the other hand, the spectral indices of NGC 1068, NGC 2992, and NGC 3516 were very similar, indicating a flat ( $\alpha > -0.5$ ) spectrum. So, their radio emission might be due to unresolved subparsec-scale winds. NGC 4593 and NGC 4388 might share a similar origin of radio emission, as they showed nearly inverted to inverted spectra ( $\alpha \geq 0$ ). In addition, these two sources showed the weakest radio emission compared to other sources in our sample. The central environment, e.g., accretion and star formation, plays a crucial role in determining the true nature of the radio emission on such a small spatial scale.

In the next few sections, we will discuss other alternate possibilities of an AGN having a steep or flat spectrum. They may be part of the bigger picture of AGN evolutionary stages or completely different AGN classes from GPS sources.

#### 4.4. Evolutionary Stages: From GPS to CSS Sources

Possible scenarios for the sources with nearly steep or steep spectra would be that they are GPS sources with lower turnover frequency, or they might be in the evolutionary stage and continue to grow from GPS to compact steep-spectrum (CSS) sources, where their turnover frequency will decrease to a few hundreds of megahertz. It is believed that the GPS sources are in the earliest stage of evolution or young radio galaxies that will eventually evolve into CSS sources on their way to becoming large radio galaxies (An & Baan 2012; O’Dea & Saikia 2021). CSS sources tend to have sizes between 500 pc and 20 kpc, while GPS sources have projected linear sizes of less than 500 pc (O’Dea & Saikia 2021). Figure 3 of FRAMEx Paper I showed C-band (4.9 GHz) hundred-parsec-scale radio morphologies from VLA observations, where we can see that NGC 1068, NGC 2992, and NGC 5506 (nearly steep/steep spectra) have kiloparsec-scale extended radio emission features (either lobe-like or diffuse structures) compared to the sources with GPS, which show much more collimated small-scale outflow features (for example, NGC 1052, NGC 3079, and NGC 4151). In Figure 4 (similar to what we have shown in Figure 2, but with a curved power-law fit), we show that NGC 1068 and NGC 2992 are examples of two possible low-turnover-frequency GPS sources that might be transient or intermittent in the evolutionary phase and will finally become a CSS source.

But a low turnover frequency indicates that NGC 1068 or NGC 2992 are older than sources like NGC 1052 or NGC 2110, whereas the opposite is true (see Section 4.5 for details). NGC 1068 has a much higher accretion rate than NGC 1052, making the central environment of NGC 1068 more chaotic and representing a younger AGN population. Though the

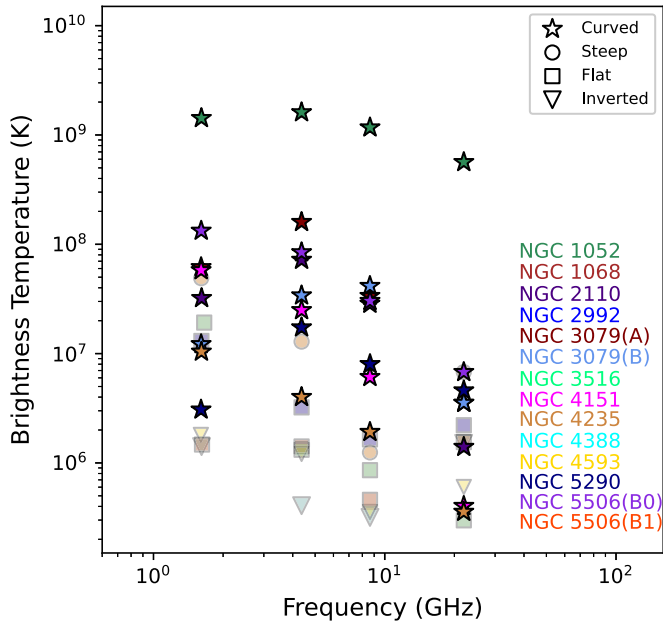


**Figure 6.** Brightness temperature (K) as a function of observed frequency (GHz). The figure shows measurements of the brightness temperature using the peak intensities at 1.6, 4.4, 8.6, and 22 GHz. The brightness temperature of the sources with gigahertz-peaked or curved spectra lies well above that of sources with flat/inverted spectra in all frequencies.

accretion rate and our study here alone cannot differentiate the actual ages of the AGNs in our sample, we believe that the nearly steep or flat-/inverted-spectra sources are examples of different classifications of (RQ) AGNs, rather than transient or specific stages of evolution between different-aged AGNs.

#### 4.5. Accretion Rate and Radio Spectra

In Figure 7 of Paper III, we showed that the radio-loudness parameter,  $R_X = L_{6\text{ cm}}/L_{2-10\text{ keV}}$ , follows a negative trend when plotted as a function of the Eddington ratio  $L_{\text{bol}}/L_{\text{Edd}}$ , which parameterizes the source’s accretion rate. Here we plot a similar figure (the left panel of Figure 5), but this time we use 4.4 GHz core flux densities (the total flux density within the  $5\sigma$  contour) instead of 6 GHz (6 cm) peak intensities to determine the radio loudness. We also show the radio spectral shape for each source we observed in this study. We find that sources with flat/inverted spectra are grouped in the region of highest accretion and lowest radio loudness, the bottom right corner of the plot. The high-accretion regime in black hole systems favors wind-based radio emission, similar to the different accretion states observed in XRBs in their transition from the “low/hard” state, associated with steady radio emission attributed to a jet, to the “high/soft” state, where the radio emission is suppressed. This wind–jet anticorrelation scenario has been discussed before in Wang et al. (2004), Sikora et al. (2007), and Mehdipour et al. (2022). This trend also appeared when we plotted the radio-loudness parameter as  $R_X = L_{8.6\text{ GHz}}/L_{2-10\text{ keV}}$ , where 8.6 GHz luminosities were measured from the total radio flux densities ( $5\sigma$ ) of our observations (Figure A1 in Appendix). If the wind is strong enough to produce shocks or outflows, the radio emission will result from the interaction between outflows and the neighboring ISM in the central region. If the wind is not strong enough or there is no ISM–wind interaction, then the radio emission from sources near or above the  $\log R_X = -4.5$  line by

Terashima & Wilson (2003), which represents the traditional separation between RL and RQ AGNs (which corresponds to a value of 10 for the optically based radio-loudness parameter  $R$ ), originates either from coronal emission or has a jet.

Based on this wind–jet scenario, we make a schematic model of the area where different physical mechanisms can dominate to produce radio emission (the right panel of Figure 5). We previously showed in Figure 8 of Paper III that the low radio luminosity of an AGN is due to a combination of the synchrotron self-absorption and the presence of wind/shocks. Here we show in our schematic that the obscuration or absorption increases for the sources with the highest accretion and lowest radio loudness (purple arrow). On the other hand, the anticorrelation between the source extension and the turnover frequency discussed in Section 4.2, as well as the conclusion from the discussion of young radio sources with relatively higher accretion rates, allows us to demonstrate that the extended collimated outflow/larger source size is associated with the lowest accretion and highest radio-loudness values (blue arrow).

#### 4.6. Star Formation at the Subparsec Scale

In a study of 62 RQ AGNs with arcsecond resolution, Smith et al. (2016) showed that radio emission (especially for sources with extended emission) in lower-resolution ( $\sim 1''$  VLA) imaging surveys might not be associated with AGN core synchrotron emission, but with star formation. A large number of previous studies of the closest Seyfert 2 galaxies suggested a link (but no direct connection) between AGNs and young star formation on a scale of a few hundred parsecs (Davies et al. 2007 and references therein). Typically, the connection between these two phenomena is discussed from kiloparsec to a few hundred parsec scales. Now, to find evidence of a stellar population in the closest proximity of AGNs (a few parsecs to subparsec scales), one approach (Middelberg et al. 2004) is to measure the proper motion of radio components close to the nucleus using multiple epochs of observations with VLBI. Middelberg et al. (2004) discussed evidence of the nonrelativistic nuclear compact radio components found in many Seyferts, mostly sources with low radio luminosities. They also suggested flat-spectrum core components for the powerful radio galaxies with a parsec-scale resolution while analyzing spectral indices. We found similar flat-/inverted-spectrum components, but associated with weak central radio-emitting sources (NGC 1068, NGC 2992, NGC 4388, and NGC 4593). These sources showed no sign of powerful, collimated, and extended features, only indicating a compact central radio emission, possibly harboring nonrelativistic star-forming components.

In addition, to extend our star formation analysis and to find any contribution from star formation to the nuclear radio emission of our sources, we calculated the radio-based (we used 1.6 GHz instead of 1.4 GHz) star formation rate (SFR) from Herrero-Illana et al. (2017, Equation (6)), which is  $\text{SFR} = 1.02 \times 10^{-28} L_{1.4\text{ GHz}}$ . The approach for determining SFR using radio data was proposed by Murphy et al. (2011) and relies on the assumption of a strong correlation between IR and radio luminosities. However, the radio luminosity at this frequency for sources with flat/inverted spectra is lower than most gigahertz-peaked sources and so is the calculated SFR. Radio emission at lower frequencies is essentially due to nonthermal emission, and we cannot distinguish the thermal

contribution using this method of calculating the SFR. On the other hand, in Figure 6, we present a plot illustrating the relationship between the brightness temperature ( $T_b$ ) and rest-frame frequency. Our findings indicate that sources with flat/inverted spectra exhibit lower  $T_b$  than those with steep and gigahertz-peaked spectra. Specifically, the  $T_b$  values for sources with flat/inverted spectra range between  $10^{6.5}$  and  $10^{5.6}$  K (in the  $C$  band). This suggests that thermal free-free emission could mainly contribute to radio emission.

## 5. Conclusions

We present results from high-resolution multiwavelength radio observations of 12 detected AGNs from our previous campaigns to look into the subparsec regime of AGNs and study their core radio emission. We obtained VLBA observations at the  $L$  ( $\sim 1.6$  GHz),  $C$  ( $\sim 4.4$  GHz),  $X$  ( $\sim 8.6$  GHz), and  $K$  ( $\sim 22$  GHz) radio bands with homogeneous observing setups. The primary goal of this paper was to determine the “True Central Origin of Radio Emission (TCORE)” and disentangle contributions from potentially multiple sources and different physical mechanisms by spectral index analysis. Our main findings are listed below.

1. We found a relatively higher detection rate ( $\sim 83\%$ ) than previous high-resolution radio studies at low frequency (the  $L$  band). All of our sources were detected in the  $C$  and  $X$  bands. On the other hand, from high-frequency  $K$ -band observations, we were able to detect  $\sim 42\%$  of our target sources. The sources with lower  $K$ -band luminosity at parsec scale suggest that synchrotron emission can still be detected in the high-frequency domain extending until or beyond 22 GHz, without any interference from the thermal emission of dust and gas.
2. We found seven GPS sources ( $\sim 60\%$ ) with a parsec- to subparsec-scale central radio-emitting region ( $\leq 1$  pc), two sources with extended outflow-like structures (NGC 1052 and NGC 4151), and two with multicomponent features (NGC 3079 and NGC 5506). The turnover frequencies or peaks of the convex spectral shape range from  $\sim 3$  to 6 GHz. Five sources showed nearly flat or inverted spectra. A component of NGC 5506 (component B1) separated by 4–5 pc from the central source showed a steep spectrum.
3. For the GPS sources, we found a linear correlation between turnover frequencies and lower frequency spectral indices or  $\alpha_1$ . This correlation means that the radio flux density drops more rapidly or gets absorbed (mainly synchrotron self-absorption in this range of frequencies) at lower frequencies for the sources with higher turnover frequencies. We established that most of our sources are mainly a group of young AGNs with dense central regions and relatively higher accretion rates. In addition, sources with flat spectra showed mostly resolved/slightly resolved bright central regions, establishing that the radio emission is from parsec-scale winds/shocks (interaction with the ISM or star formation). On the other hand, sources with steep spectra may

produce radio emission from a small-scale, optically thin, one-sided, strong collimated outflow.

4. A higher accretion rate favors wind-based radio emission in AGNs, similar to the different accretion states observed in XRBs transitioning from the “low/hard” state to the “high/soft” state, where the radio emission is suppressed. We found that sources with flat/inverted spectra are grouped in the region of highest accretion and lowest radio luminosity, supporting the idea of wind-based radio emission or interaction between outflows and the neighboring ISM in the central region.
5. A thermal free-free emission from an optically thick region in the immediate vicinity of a black hole may be the primary source of the radio emission for the sources with flat/inverted spectra. The lower range of brightness temperatures, especially in the  $K$ -band or higher-frequency regime, ranges between  $10^{6.2}$  K  $\geq T_b \geq 10^{5.2}$  K, suggesting compact central radio emission possibly harboring nonrelativistic star-forming or thermal radio-emitting components.

VLBA high-resolution and multiwavelength observations at radio energies have allowed us to provide insights into a critical aspect of the overall emission mechanisms of these AGNs. Our next goal is a high-resolution  $K$ -band monitoring project of a large sample of nearby AGNs, which could be crucial to identifying the true central origin (and nature) of radio emission (TCORE). A future study using an even more powerful radio telescope, such as the higher-frequency Event Horizon Telescope or Atacama Large Millimeter Array, would be useful to constrain the particle acceleration mechanisms in the near-horizon environments of the SMBHs in galaxy centers.

## Acknowledgments

This work supports USNO’s ongoing research into the celestial reference frame and geodesy.

The National Radio Astronomy Observatory is a facility of the National Science Foundation operated under a cooperative agreement by Associated Universities, Inc. The authors acknowledge the use of the Very Long Baseline Array under the US Naval Observatory’s time allocation. This work made use of data supplied by the UK Swift Science Data Centre at the University of Leicester.

*Facilities:* VLBA, Swift.

*Software:* AIPS, Astropy (Astropy Collaboration et al. 2013, 2018), CASA (CASA Team et al. 2022).

## Appendix Additional Plots

In Figure A1, we plot radio loudness versus the Eddington ratio, using the radio-loudness parameter as  $R_X = L_{6\text{ GHz}}/L_{2-10\text{ keV}} \& L_{8.6\text{ GHz}}/L_{2-10\text{ keV}}$ , where 6 GHz luminosities were calculated using the peak intensities (Papers I and III) and 8.6 GHz luminosities were measured from the total radio flux densities ( $5\sigma$ ) of our observations (this work).



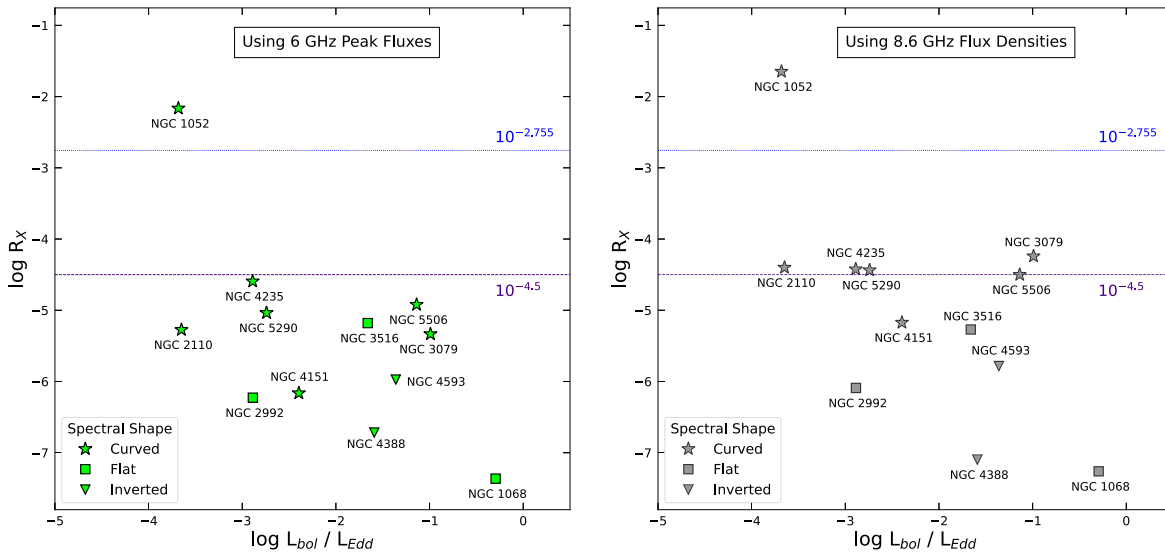


**Figure A1.** The same as Figure 5, but with 6 GHz peak intensities (left) and 8.6 GHz flux densities from the  $5\sigma$  contour region (right).

### ORCID iDs

Onic I. Shuvo <https://orcid.org/0000-0003-4727-2209>  
 Megan C. Johnson <https://orcid.org/0000-0002-4146-1618>  
 Nathan J. Secrest <https://orcid.org/0000-0002-4902-8077>  
 Mario Gliozzi <https://orcid.org/0000-0002-8818-9009>  
 Phillip J. Cigan <https://orcid.org/0000-0002-8736-2463>  
 Travis C. Fischer <https://orcid.org/0000-0002-3365-8875>  
 Alexander J. Van Der Horst <https://orcid.org/0000-0001-9149-6707>

### References

- An, T., & Baan, W. A. 2012, *ApJ*, **760**, 77  
 Antonucci, R. 1993, *ARA&A*, **31**, 473  
 Astropy Collaboration, Price-Whelan, A. M., Sipőcz, B. M., et al. 2018, *AJ*, **156**, 123  
 Astropy Collaboration, Robitaille, T. P., Tollerud, E. J., et al. 2013, *A&A*, **558**, A33  
 Baczko, A. K., Ros, E., Kadler, M., et al. 2022, *A&A*, **658**, A119  
 Baldi, R. D., Williams, D. R. A., McHardy, I. M., et al. 2018, *MNRAS*, **476**, 3478  
 CASA Team, Bean, B., Bhatnagar, S., et al. 2022, *PASP*, **134**, 114501  
 Charlot, P., Jacobs, C. S., Gordon, D., et al. 2020, *A&A*, **644**, A159  
 Cheng, X., An, T., Wang, A., & Jaiswal, S. 2023, *Galax*, **11**, 42  
 Coriat, M., Corbel, S., Prat, L., et al. 2011, *MNRAS*, **414**, 677  
 Davies, R. I., Müller Sánchez, F., Genzel, R., et al. 2007, *ApJ*, **671**, 1388  
 de Vries, W. H., Barthel, P. D., & O'Dea, C. P. 1997, *A&A*, **321**, 105  
 Dorland, B., Secrest, N., Johnson, M., et al. 2020, in Proc. of the Journées 2019, “Astrometry, Earth Rotation, and Reference Systems in the GAIA era”, ed. C. Bizouard, **165**  
 Fanti, R., Fanti, C., Schilizzi, R. T., et al. 1990, *A&A*, **231**, 333  
 Fernandez, L. C., Secrest, N. J., Johnson, M. C., et al. 2022, *ApJ*, **927**, 18  
 Fischer, T. C., Secrest, N. J., Johnson, M. C., et al. 2021, *ApJ*, **906**, 88  
 Gültekin, K., Cackett, E. M., Miller, J. M., et al. 2009, *ApJ*, **706**, 404  
 Gültekin, K., Nyland, K., Gray, N., et al. 2022, *MNRAS*, **516**, 6123  
 Herrero-Illana, R., Pérez-Torres, M. Á., Randriamanakoto, Z., et al. 2017, *MNRAS*, **471**, 1634  
 Hovatta, T., Aller, M. F., Aller, H. D., et al. 2014, *AJ*, **147**, 143  
 Hutchings, J. B., Janson, T., & Neff, S. G. 1989, *ApJ*, **342**, 660  
 Ishibashi, W., & Courvoisier, T. J. L. 2011, *A&A*, **525**, A118  
 Kamenó, S., Inoue, M., Wajima, K., Sawada-Satoh, S., & Shen, Z.-Q. 2003, *PASA*, **20**, 134  
 Lister, M. L. 2003, in ASP Conf. Ser. 300, Radio Astronomy at the Fringe, ed. J. A. Zensus, M. H. Cohen, & E. Ros (San Francisco, CA: ASP), **71**  
 Maini, A., Prandoni, I., Norris, R. P., Giovannini, G., & Spitler, L. R. 2016, *A&A*, **589**, L3  
 Martí-Vidal, I., Ros, E., Pérez-Torres, M. A., et al. 2010, *A&A*, **515**, A53  
 Mehdipour, M., Kriss, G. A., Brenneman, L. W., et al. 2022, *ApJ*, **925**, 84  
 Merloni, A., Heinz, S., & di Matteo, T. 2003, *MNRAS*, **345**, 1057  
 Middelberg, E., Roy, A. L., Nagar, N. M., et al. 2004, *A&A*, **417**, 925  
 Miller, L., Peacock, J. A., & Mead, A. R. G. 1990, *MNRAS*, **244**, 207  
 Murphy, E. J., Condon, J. J., Schinnerer, E., et al. 2011, *ApJ*, **737**, 67  
 O'Dea, C. P. 1998, *PASP*, **110**, 493  
 O'Dea, C. P., & Baum, S. A. 1997, *AJ*, **113**, 148  
 O'Dea, C. P., Baum, S. A., & Stanghellini, C. 1991, *ApJ*, **380**, 66  
 O'Dea, C. P., & Saikia, D. J. 2021, *A&ARv*, **29**, 3  
 Panessa, F., Baldi, R. D., Laor, A., et al. 2019, *NatAs*, **3**, 387  
 Panessa, F., Barcons, X., Bassani, L., et al. 2007, *A&A*, **467**, 519  
 Panessa, F., Chiaraluce, E., Bruni, G., et al. 2022, *MNRAS*, **515**, 473  
 Patil, P., Nyland, K., Harwood, J. J., Kimball, A., & Mukherjee, D. 2018, in ASP Conf. Ser. 517, Science with a Next Generation Very Large Array, ed. E. Murphy (San Francisco, CA: ASP), **595**  
 Patil, P., Nyland, K., Whittle, M., et al. 2020, *ApJ*, **896**, 18  
 Sawada-Satoh, S., Kamenó, S., Nakamura, K., et al. 2008, *ApJ*, **680**, 191  
 Shuvo, O. I., Johnson, M. C., Secrest, N. J., et al. 2022, *ApJ*, **936**, 76  
 Sikora, M., Stawarz, L., & Lasota, J.-P. 2007, *ApJ*, **658**, 815  
 Smith, K. L., Mushotzky, R. F., Koss, M., et al. 2020, *MNRAS*, **492**, 4216  
 Smith, K. L., Mushotzky, R. F., Vogel, S., Shimizu, T. T., & Miller, N. 2016, *ApJ*, **832**, 163  
 Snellen, I. A. G., Schilizzi, R. T., de Bruyn, A. G., et al. 1998, *A&AS*, **131**, 435  
 Sotnikova, Y. V., Mufakharov, T. V., Majorova, E. K., et al. 2019, *AstBu*, **74**, 348  
 Tadhunter, C. 2016, *A&ARv*, **24**, 10  
 Terashima, Y., & Wilson, A. S. 2003, *ApJ*, **583**, 145  
 Tinti, S., Dallacasa, D., de Zotti, G., Celotti, A., & Stanghellini, C. 2005, *A&A*, **432**, 31  
 Trotter, A. S., Greenhill, L. J., Moran, J. M., et al. 1998, *ApJ*, **495**, 740  
 Ulvestad, J. S., Wong, D. S., Taylor, G. B., Gallimore, J. F., & Mundell, C. G. 2005, *AJ*, **130**, 936  
 van Moorsel, G., Kembell, A., & Greisen, E. 1996, in ASP Conf. Ser. 101, Astronomical Data Analysis Software and Systems V, ed. G. H. Jacoby & J. Barnes (San Francisco, CA: ASP), **37**  
 Wang, J.-M., Luo, B., & Ho, L. C. 2004, *ApJL*, **615**, L9  
 Williams, D. R. A., Baldi, R. D., McHardy, I. M., et al. 2020, *MNRAS*, **495**, 3079  
 Williams, D. R. A., McHardy, I. M., Baldi, R. D., et al. 2017, *MNRAS*, **472**, 3842